Phosphorylated paxillin and phosphorylated FAK constitute subregions within focal adhesions

Bachmann, Michaël; Skripka, Artiom; Weißenbruch, Kai; Wehrle-Haller, Bernhard; Bastmeyer, Martin

How to cite

BACHMANN, Michaël et al. Phosphorylated paxillin and phosphorylated FAK constitute subregions within focal adhesions. In: Journal of cell science, 2022, vol. 135, n° 7, p. jcs258764. doi: 10.1242/jcs.258764

This publication URL: https://archive-ouverte.unige.ch/unige:163579
Publication DOI: 10.1242/jcs.258764

© 2022. Published by The Company of Biologists Ltd | Journal of Cell Science (2022) 135, jcs258764. doi:10.1242/jcs.258764

RESEARCH ARTICLE

Phosphorylated paxillin and phosphorylated FAK constitute subregions within focal adhesions

Michael Bachmann[1,2,§], Artiom Skripka[2,*,‡], Kai Weißenbruch[2,3], Bernhard Wehrle-Haller[1] and Martin Bastmeyer[2,4]

ABSTRACT

Integrin-mediated adhesions are convergence points for multiple signaling pathways. Their inner structure and diverse functions can be studied with super-resolution microscopy. Here, we examined the spatial organization within focal adhesions by analyzing several adhesion proteins with structured illumination microscopy (SIM). Paxillin (Pax) serves as a scaffold protein and signaling hub in focal adhesions, and focal adhesion kinase (FAK, also known as PTK2) regulates the dynamics of adhesions. We found that their phosphorylated forms, pPax and pFAK, form spot-like, spatially defined clusters within adhesions in several cell lines and confirmed these findings with additional super-resolution techniques. These clusters showed a more regular separation from each other compared with more randomly distributed signals for FAK or paxillin. Mutational analysis indicated that the active (open) FAK conformation is a prerequisite for the pattern formation of pFAK. Live-cell super-resolution imaging revealed that organization in clusters is preserved over time for FAK constructs; however, distance between clusters is dynamic for FAK, while paxillin is more stable. Combined, these data introduce spatial clusters of pPax and pFAK as substructures in adhesions and highlight the relevance of paxillin–FAK binding for establishing a regular substructure in focal adhesions.

KEY WORDS: Focal adhesions, Paxillin, Paxillin phosphorylation, FAK, Super-resolution microscopy

INTRODUCTION

Integrin-mediated adhesions between cells and the surrounding extracellular matrix are not only important for physical anchorage, but are also points of convergence for different intracellular and extracellular signals (Bachmann et al., 2019; Conway and Jacquemet, 2019; Green and Brown, 2019). These adhesions consist of a plethora of structural and signaling proteins establishing the 'adhesome' (Byron et al., 2011; Kuo et al., 2011; Schiller et al., 2011). Based on adhesome studies, a meta-analysis curated a consensus adhesome in which the members form functional clusters connected with each other into a complex network (Horton et al., 2015). The advent of super-resolution microscopy confirmed these functional clusters by showing that members of a given cluster are organized within a specific functional layer in the axial direction (Kanchanawong et al., 2010). In lateral directions, pointillistic super-resolution methods and stimulated emission depletion (STED) microscopy revealed the existence of a substructure of small individual clusters within adhesions (Bachmann et al., 2016; Changede et al., 2015; Diez-Ahedo et al., 2009; Shroff et al., 2008, 2007; Xu et al., 2018). Some studies successfully attributed functional aspects to these lateral clusters (Spiess et al., 2018), but the structure-function relationship along lateral directions in focal adhesions remains less studied.

One of the most important proteins for the structure and function of integrin-mediated adhesions is paxillin (Pax or PXN). Paxillin is part of the LIM-domain protein family and is recruited to adhesions by integrins and their activators, talin and kindlin (Pinon et al., 2014; Theodosiou et al., 2016), potentially facilitated by membrane interaction of the LIM4 domain of paxillin (Ripamonti et al., 2021). Integrin activation and integrin-mediated cell adhesion can occur in the absence of paxillin but cell spreading and proliferation relies on paxillin recruitment to integrin adhesions (Pinon et al., 2014; Soto-Ribeiro et al., 2019). Structurally, paxillin serves as a scaffold protein and its multiple binding partners are regulated by paxillin phosphorylation (Deakin and Turner, 2008). Tyrosine phosphorylation at Y31 (pPax-Y31) and Y118 (pPax-Y118) by a complex of focal adhesion kinase (FAK, also known as PTK2) and Src has been intensively studied and recruits activators and inhibitors for Rho-GTPases (Deakin and Turner, 2008; Petit et al., 2000; Schaller and Parsons, 1995; Thomas et al., 1999). These phospho-tyrosine sites are also important for adhesion dynamics (Ripamonti et al., 2021; Zaidel-Bar et al., 2007) and vinculin recruitment (Pasapera et al., 2010). The adhesome studies mentioned above cluster FAK and paxillin within the same functional group (Horton et al., 2015). Moreover, paxillin and FAK localize in the same *z*-layer (Kanchanawong et al., 2010) and form a complex, preferentially when paxillin is phosphorylated at Y31 and Y118 (Choi et al., 2011; Digman et al., 2008).

FAK contains an N-terminal FERM domain, followed by a kinase, an unstructured region and a focal adhesion targeting (FAT) domain. In the inactive state, the FERM and kinase domains bind to each other, and this inhibition is released by trans-autophosphorylation of FAK-Y397 (Acebrón et al., 2020). FAT binding to paxillin is necessary and sufficient for focal adhesion localization of FAK (Deramaudt et al., 2014). Simultaneous binding of FAK to membrane lipids and to paxillin is proposed to put FAK under mechanical strain, and to increase activation (Seong et al., 2013; Torsoni et al., 2003; Wong et al., 2011) and kinase activity of

---

[1]Department for Cell Physiology and Metabolism, University of Geneva, Rue Michel-Servet 1, 1211 Geneva, Switzerland. [2]Zoological Institute, Cell- and Neurobiology, Karlsruhe Institute of Technology (KIT), Fritz-Haber-Weg 4, 76131 Karlsruhe, Germany. [3]Institute of Functional Interfaces (IFG), Karlsruhe Institute of Technology (KIT), 76128 Karlsruhe, Germany. [4]Institute for Biological and Chemical Systems – Biological Information Processing (IBCS-BIP), Karlsruhe Institute of Technology (KIT), 76344 Eggenstein-Leopoldshafen, Germany.
*Present address: Nanomaterials for Bioimaging Group, Departamento de Física de Materiales, Facultad de Ciencias, Universidad Autónoma de Madrid, Madrid, 28049 Spain. ‡Present address: The Molecular Foundry, Lawrence Berkeley National Laboratory, Berkeley, CA 94720, USA.

§Author for correspondence (michael.bachmann@unige.ch)

M.B., 0000-0001-9450-3458; A.S., 0000-0003-4060-4290; B.W., 0000-0002-1159-1147

Handling Editor: Kathleen Green
Received 8 April 2021; Accepted 17 March 2022

FAK (Bauer et al., 2019). Phosphorylated FAK-Y397 not only activates FAK but also recruits Src, highlighting the scaffolding function of FAK that might be more relevant than its kinase function (Arold, 2011). Accordingly, blocking the kinase activity of Src, but not of FAK, largely inhibits paxillin phosphorylation at Y118 (Horton et al., 2016), highlighting again the relevance of Src for the actual phosphorylation of focal adhesion proteins.

Here we studied the lateral organization of several adhesome proteins within integrin-mediated adhesions using different optical microscopy super-resolution techniques. We analyzed proteins belonging to different functional clusters or axial (*z*-) layers and found different patterns of spatial distribution of adhesome proteins within the same adhesion. Most proteins, including paxillin, were distributed continuously throughout an adhesion, while phosphorylated paxillin (pPax) and activated FAK showed enrichment in distinct clusters. Moreover, we detected these spots in different cell lines and showed with super-resolution live-cell imaging that the lateral mobility of spots within adhesions depends on FAK conformation. Finally, we demonstrated that this spacing is modulated by contractility and vinculin.

RESULTS

Substructure of adhesome proteins in focal adhesions

Rat embryonic fibroblast (REF) cells are an established cell line for the analysis of adhesions and their composition (Cavalcanti-Adam et al., 2007; Franz and Müller, 2005; Gudzenko and Franz, 2015; Hoffmann et al., 2014). We cultured these cells on fibronectin-coated coverslips and transfected fluorescently tagged proteins of interest or performed secondary immunolabeling to analyze several consensus adhesome proteins. We tested: (i) two different integrins [GFP-tagged β3 (ITGB3) and BMB5 antibody against α5 (ITGA5), staining αVβ3 and α5β1, respectively]; (ii) talin-1 and kindlin-2 (also known as TLN1 and FERMT2, respectively; integrin-activating adapters); (iii) paxillin, FAK and pPax-Y118 (signaling adapters); (iv) vinculin and zyxin (Vin or VCL, and ZYX, respectively; actin binders); and (v) actin itself. Imaging was performed with SIM, allowing us to analyze the organization of focal adhesions with twice the resolution compared with diffraction-limited microscopic methods (Bachmann et al., 2016). Admittedly, SIM does not resolve single fluorophores. Thus, structures visible in SIM represent local agglomerations (clusters) of several fluorophores, while structures labeled with one or very few fluorophores might be disregarded as background in contrast to more sensitive microscopic methods.

To analyze the spatial organization of adhesome proteins inside single cell–matrix adhesions, we focused on focal adhesions (Gardel et al., 2010). With the experimental conditions we used, we rarely observed fibrillar adhesions, while nascent adhesions or focal complexes were too small to manifest a sub-structural organization that could be detected with SIM. Using SIM, we could confirm earlier observations that focal adhesions are split into parallel ‘stripes’ (as indicated, for example, by the paxillin staining in Fig. 1), compared with a more homogenous organization observed with diffraction-limited microscopy (Hu et al., 2015; Young and Higgs, 2018). We found that these stripes were well separated from each other, and could be considered as individual focal adhesions in our experimental setup. A closer analysis of protein localization in these focal adhesions revealed that some adhesome proteins were organized in substructures that were well separated from each other. Intensity profiles along the long axis of focal adhesions gave the impression that, for example, pPax-Y118 was segregated into separate clusters within the same adhesion. Moreover, pPax-Y118 spots showed a remarkable regularity concerning the spacing of these clusters. In contrast, labeling intensities of paxillin, vinculin, zyxin and actin varied along the focal adhesions, but were almost continuously present throughout their whole lengths. Spatially separated clusters were only visible occasionally and not as regularly as observed for pPax-Y118. Fluorescent labeling of the remaining proteins – α5β1 and αVβ3 integrin, talin-1 and kindlin-2 – revealed a behavior somewhat

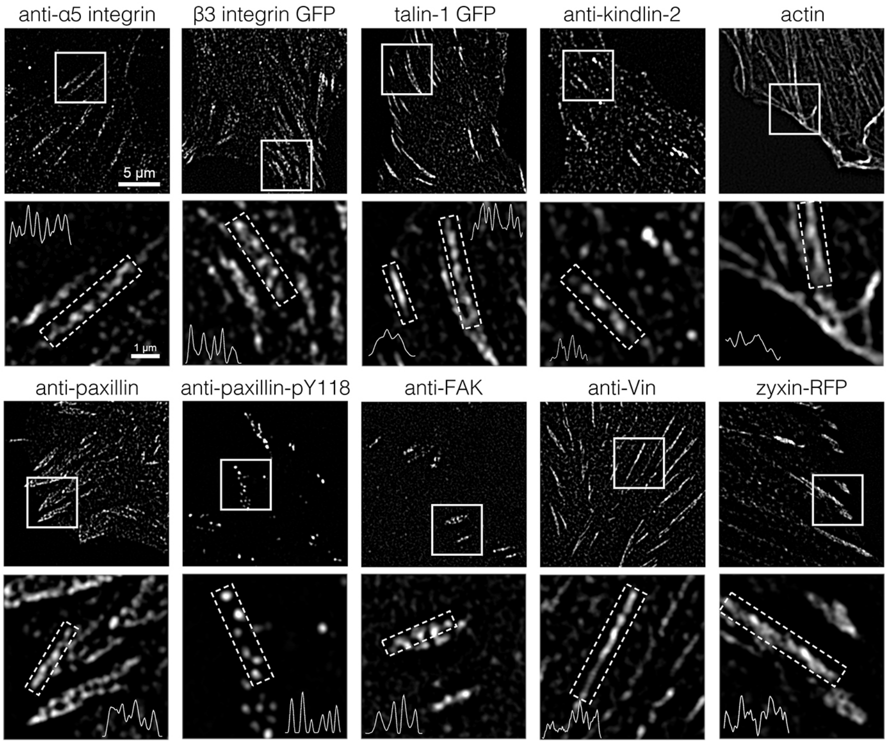

Fig. 1. Analysis of spatial distribution of adhesome proteins within focal adhesions. Rat embryonic fibroblasts (REFs) were cultured on fibronectin-coated coverslips. Cells were transfected for the indicated protein or labeled with antibodies or with phalloidin for actin, and analyzed for fluorescence. White boxes indicate magnified regions shown below. Intensity profiles of focal adhesions are shown as dashed white rectangles in the magnified images. Note that variations along the intensity profiles are observed for all proteins. However, some conditions revealed distinct intensity spots indicating separated protein clusters. Scale bars: 5 µm in overview, 1 µm in magnified images. Images are representative of three experiments.

between the two cases mentioned above. This is highlighted by the magnified panel for talin-1 in Fig. 1 which shows focal adhesions with continuous and spot-like organizations of talin-1 next to each other.

Thus, SIM gave the impression of spatial distributions within focal adhesions that differed between different adhesome proteins but also depended on the phosphorylation status, as shown for pPax-Y118 in comparison to paxillin.

Phosphorylated paxillin organizes in clusters with regular spacing to each other

Surprised by the difference in the paxillin and pPax-Y118 staining patterns, we decided to analyze their spatial organization in a quantitative manner. We labeled endogenous paxillin in REFs, as well as pPax-Y118 (Fig. 2A). Magnifications of single focal adhesions confirmed our earlier observation that paxillin is organized rather homogenously throughout adhesions, while pPax-Y118 localized in discrete clusters (Fig. 2A′–A‴). To analyze differences between spatial distribution of paxillin and pPax-Y118, we applied two independent methods to detect intensity peaks and to measure distances between these peaks. We used a published ImageJ-based plugin (NanoJ Core, Laine et al., 2019) to measure nearest-neighbor (NN) distances and independently developed a custom-written MATLAB routine that measures the center-to-center distance of the intensity maxima of labeled proteins (Fig. S1A). Using both methods, we analyzed our SIM images of pPax-Y118 and performed an analysis of paxillin labeling using the NN method as reference. From these distance values, we created histograms and plotted the average distance distribution based on histograms from independent experiments (Fig. 2B). These distance distribution plots revealed a narrower distance distribution of pPax-Y118 intensity peaks compared with that of paxillin and a peak distance that was shifted towards shorter distances for pPax-Y118. A quantitative comparison confirmed the impression of shorter distances between pPax-Y118 maxima (Fig. 2C; 555 nm with NN measurements and 469 nm with our MATLAB-based algorithm) compared with paxillin (616 nm). The distance distribution of pPax-Y118 also appeared more centered around the peak indicating less variation in distances between intensity maxima. We quantified the full-width half-maxima (FWHM) of distance distributions (Fig. 2D), which indeed revealed significantly smaller FWHM for pPax-Y118 compared with paxillin. Our MATLAB code also allowed us to measure the diameters of detected spots (Fig. 2E; paxillin, 332 nm; pPax-Y118, 267 nm) and to plot the number of detected spots within an adhesion against the length of that adhesion (Fig. 2F). Additionally, we tested the spatial distribution of vinculin (Fig. S1B–D) and found that the distances between vinculin maxima were broadly distributed, similar to those of paxillin.

Overall, these data and their analyses showed that pPax-Y118 forms ‘spots’ or spatially constrained clusters. These clusters are closer to each other and have a more regular spacing compared with clusters analyzed for paxillin. We believe that these analyses correspond well with the visual impressions from Fig. 1 and Fig. 2A, and show that pPax-Y118 has a stronger tendency to be constrained in clusters whereas paxillin and vinculin seem to lack a well-defined pattern within adhesions.

Additionally, to confirm that the differences in spatial distribution were not induced by labeling artefacts, we performed titration

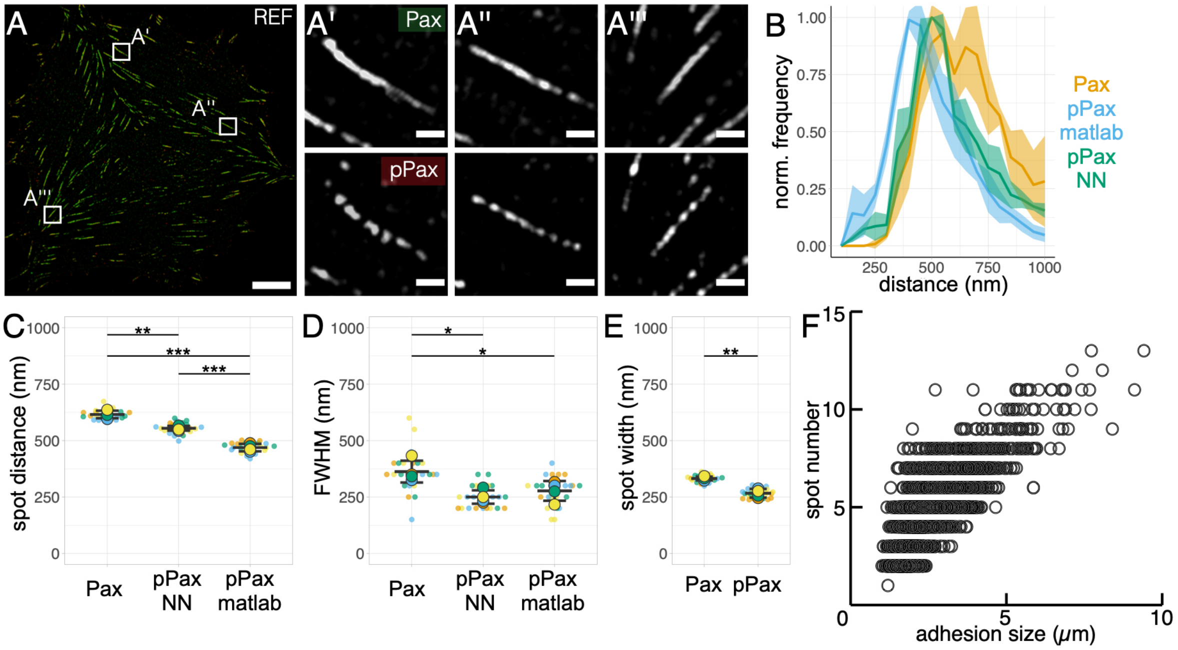

Fig. 2. Analysis of inner organization of focal adhesions for paxillin and pPax-Y118. (A) REF cells cultured on fibronectin-coated coverslips and labeled for paxillin (green) and pPax-Y118 (red). Images are representative of four experiments. Scale bars: 10 µm in overview, 1 µm in magnified images. (B) Quantitative analysis of distances between intensity maxima. Distances as histogram (bin width 50 nm) showed different distance distributions for pPax-Y118 (analyzed with two independent methods) compared with paxillin. Highest bin for each condition was set to one. Thick line indicates mean values from *n*=4 independent experiments and shades around mean indicate 95% confidence intervals. Non-overlapping regions indicate significant differences. (C) Mean distance values between identified maxima of respective labeling and method (NN for paxillin). Big dots: mean values from independent experiments (*n*=4); small dots: number of cells (*n*=24; in total >10,000 distances measured); central bar indicates mean, standard deviation above and below. (D) FWHM of histograms calculated based on number of bins with normalized frequency ≥0.5. (E) Diameter values for spots identified with MATLAB workflow. (F) Distribution of the number of clusters within a single adhesion versus the length of the respective adhesion. Every dot represents one adhesion. Significance was tested between all conditions based on independent experiments with Welch's *t*-test after testing for normal distribution with Shapiro–Wilk test. *0.05≥*P*>0.01; **0.01≥*P*>0.001; ***$P\leq0.001$.

experiments of primary antibodies for paxillin (Fig. S2E–H) and pPax-Y118 (Fig. S2A–D). We could not detect a concentration-dependent effect of antibodies on the rather homogenous appearance of paxillin compared with the spot-like pPax-Y118 staining. We also tested a primary antibody for pPax-Y118 from another supplier and an antibody for pPax-Y31 (Fig. S2A–D). Both antibodies against pPax-Y118 confirmed the observation that pPax-Y118 organizes within separable spatial clusters, as does pPax-Y31.

pPax-Y118 organizes in spatially separated clusters in several cell lines

Next, we tested whether the observation of pPax-Y118 confinement in spatially separated clusters can be extended to different cell lines. We compared other established fibroblast cell lines (mouse embryonic fibroblasts, MEFs; mouse fibroblasts, NIH3T3; primary human foreskin fibroblasts, HFFs), a cancer cell line (HeLa) and an epithelial cell line (normal rat kidney cells, NRKs) (Fig. 3). In all cell lines, pPax-Y118 showed a distribution in separated clusters in contrast to the more homogenous paxillin staining (Fig. 3A). Quantitative analyses with our MATLAB workflow revealed that pPax-Y118 cluster spacing is overall conserved between different cell lines (Fig. 3B). This was also true for HeLa and HFF cells that differed the most regarding their maximum adhesion lengths (Fig. 3A,C). A histogram plot of distance distributions also confirmed that distances of pPax-Y118 clusters did not vary significantly between these cell lines and REF cells (Fig. 3D).

Phosphorylated tyrosines in focal adhesions organize in clusters

Paxillin is phosphorylated at Y31 and Y118 by a FAK–Src complex that forms after the activation of FAK by Y397 auto-phosphorylation (Arold et al., 2001; Sulzmaier et al., 2014; Thomas et al., 1998). We decided to test whether pFAK shows a spatial behavior that is similar to pPax-Y118 and paxillin. First, we labeled all combinations of these proteins in REF cells, imaged them with AiryScan microscopy (Jacquemet et al., 2020), and analyzed their intensity correlation and spatial co-occurrence (Pearson correlation and Mander coefficients; see also Aaron et al., 2018). These analyses confirmed high correlation and high co-occurrence of both FAK and paxillin with their phosphorylated versions (Fig. S3), and thereby a close interaction between both proteins. Next, we labeled focal adhesions in REF cells for pFAK (Fig. 4B) as well as for pPax-Y118 as a control (Fig. 4A) and imaged them with SIM. These images revealed that pFAK (Fig. 4B) is spatially organized in clusters as seen before for pPax-Y118. We then labeled focal adhesions with primary antibodies that bind promiscuously to phosphorylated tyrosines (pTyr; Fig. 4C), which also revealed a spatial pattern of separated clusters. Finally, we used these data and performed a quantitative NN analysis as done before for pPax-Y118 and paxillin. Histograms of NN distances showed spacings of pFAK and pTyr that closely followed that of pPax (Fig. 4D), albeit slightly shifted to smaller distances (Fig. 4E; pFAK, 483 nm; pTyr, 530 nm). Measurements of FWHM for pTyr and pFAK (Fig. 4F) confirmed the impression from distance distribution plots that

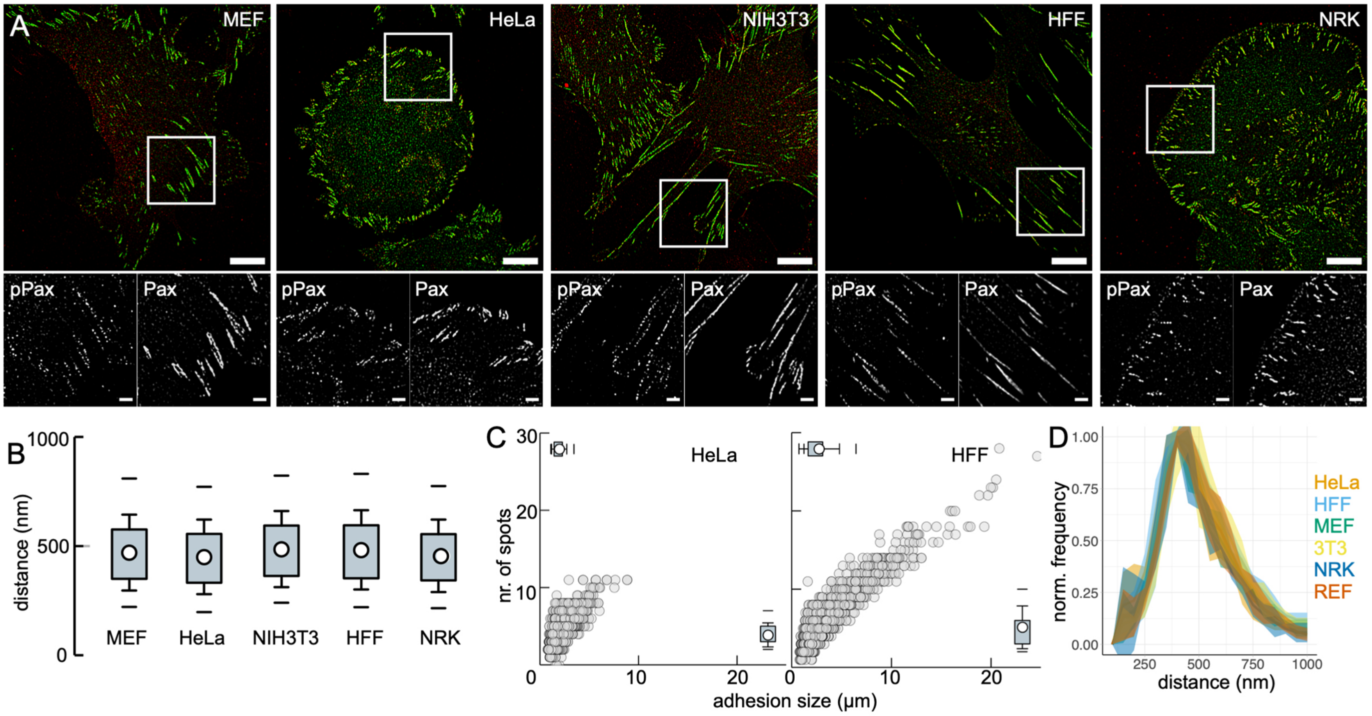

Fig. 3. pPax-Y118 organizes in spots in several different cell lines. (A) Cancer cells (HeLa), mesenchymal cells [mouse fibroblasts (NIH3T3), mouse embryonic fibroblasts (MEFs) and human foreskin fibroblasts (HFFs)] and epithelial cells [normal rat kidney cells (NRKs)] were labeled with indirect immunostaining for paxillin (green) and pPax-Y118 (red). Magnifications showed continuous distribution of paxillin while pPax-Y118 was constrained in distinct spots. Images are representative of at least three experiments. Scale bars: 10 µm for overview images, 2 µm for magnified images. (B) Distance analysis of neighbored pPax-Y118 spots (MATLAB workflow) and (C) spot number versus adhesion length plot for HeLa and HFF cells both revealed comparable distribution of pPax [*n*=3 (NIH3T3, NRK) or 4 (HeLa, HFF, MEF) independent experiments; 18 cells per cell line or more analyzed]. (D) Histograms of pPax-Y118 distance distributions (REF data replotted from Fig. 2B). Significance compared to REF data (from Fig. 2B, pPax-Y118 MATLAB) was tested based on independent experiments with Welch's *t*-test after testing for normal distribution with Shapiro–Wilk test. No significant differences were found.

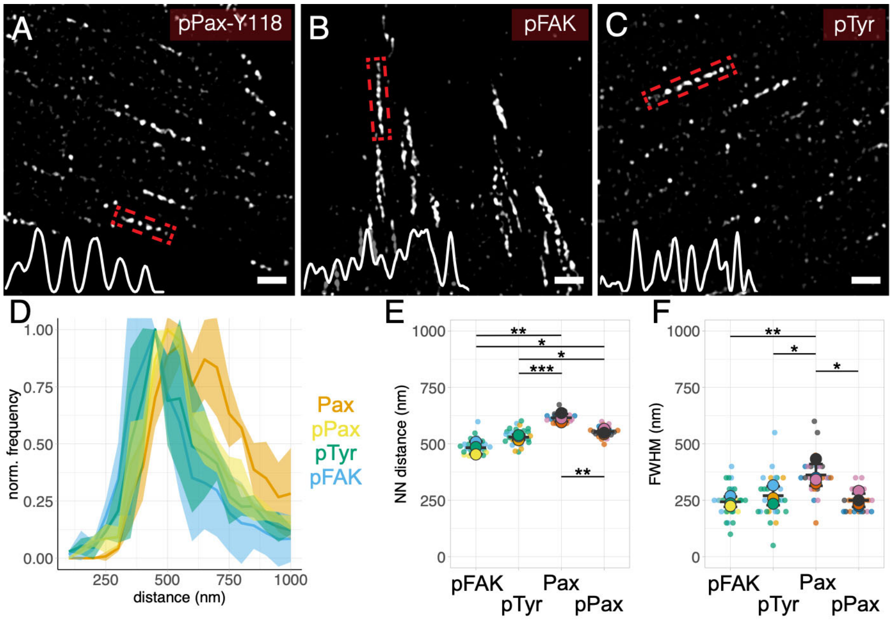

Fig. 4. Confinement in separated clusters is observed for adhesome proteins with phosphorylated tyrosines. (A–C) Magnified images with intensity profile for REF cells labeled for pPax-Y118 (A), pFAK (B) and pTyr (C) (line profile from dotted red box). Images are representative of three experiments. Scale bars: 2 µm. (D) Distance distribution analysis of pFAK (*n*=3 experiments, *n*=38 cells) and pTyr (*n*=3 experiments, *n*=38 cells) compared with data for paxillin and pPax-Y118 from Fig. 2B (all NN analysis). (E) Average NN distances for indicated conditions and (F) FWHM values from distance distribution plots. Significance was tested between all conditions based on independent experiments with Welch's *t*-test after testing for normal distribution with Shapiro–Wilk test. *0.05≥*P*>0.01; **0.01≥*P*>0.001; ***$P \leq 0.001$.

the distances between clusters of these phosphorylated proteins followed a more regular distribution as observed before for pPax-Y118, in contrast to the more homogenous paxillin labeling.

Finally, we tested pFAK organization in NIH3T3 cells with STED microscopy (Fig. S4). We used different intensities of the depletion laser to mimic confocal microscopy (0% depletion laser) and SIM microscopy (5% depletion laser) or used a higher intensity to detect pFAK clusters with a better resolution than we did before (15% depletion laser). The distances between pFAK clusters were comparable to those measured before, but decreased slightly with increasing STED resolution (Fig. S4B,C; pFAK distances were 466 nm, 415 nm, 348 nm for 0%, 5%, 15% depletion laser, respectively). Upon visual inspection, it seemed that a higher resolution resolved comparably dim structures that were lost as background in the case of SIM imaging or STED at a lower resolution (Fig. S4A,D; example indicated with arrow). We tested this by creating an adhesion mask based on pFAK images resolved at 0% STED and applied this mask to 0%, 5% and 15% STED images (Fig. S4E). The fluorescent intensity found within this mask was comparable and showed that the improved resolution did not resolve relevant additional amounts of labeled pFAK in this setting. This also fit to intensity profiles as shown in Fig. S4D where the highest intensity maxima fully overlapped for all three STED imaging conditions whereas only the dimer regions differed depending on the resolution limit. Based on the STED results, we propose that spatial distribution of pFAK is not strictly binary as it might appear from images at lower resolution. However, clusters resolved at lower resolution contained the majority of the fluorescent intensity and thereby labeled protein. This also implies that the differences in distance distribution that we observed are representative of the majority of the respective proteins in adhesions.

FAK conformation regulates spacing of FAK clusters

Next, we wanted to study FAK and pFAK in more detail and specifically if we could identify protein domains of FAK or conformations of FAK that are linked to the specific spatial distribution of pFAK. To do so, we transfected NIH3T3 cells with plasmids encoding FAK wild type (wt) or different mutations of FAK and imaged them with AiryScan microscopy (Fig. 5A). Additionally, we labeled these cells for endogenous paxillin and for pFAK. We tested the following mutations of FAK: (i) a dominant-negative form without the kinase domain (FAK dKin), (ii) FAK that is not activatable (FAK Y397F), (iii) a double mutant combining FAK dKin with Y397F (FAK dKin Y397F), (iv) the isolated FAT domain (FAK FAT) or (v) a chimera of a membrane-targeted fluorophore, connected with a flexible linker to FAT (mFAT). This chimera connects to the lipid membrane within focal adhesions but lacks kinase activity, Src recruitment and specificity for phosphatidylinositol-4,5-bisphosphate (PIP2). Images of cells expressing these FAK constructs showed that all FAK constructs localized in focal adhesions (Fig. 5A, second row) together with endogenous paxillin (Fig. 5A, first row). Pearson correlation analysis showed that the intensities of all FAK versions correlated to similar degrees with the intensity of endogenous paxillin (Fig. 5B). The Pearson correlation with pFAK (Fig. 5C) was low for mutants lacking a functional FAK Y397 phosphorylation site (FAK Y397F, FAK dKin Y397F, FAT and mFAT) and high for those with the Y397 site (FAK wt and FAK dKin). This result is in line with the significant reduction of pFAK intensity for FAK dKin Y397F, FAK FAT and mFAT (Fig. 5D).

Next, we again used NN analysis and analyzed the spatial distributions of all labeled protein species. This analysis revealed shorter NN distances for pFAK compared with those of paxillin and FAK wt (Fig. 5E; paxillin, 501 nm; pFAK, 359 nm; FAK wt, 467 nm). These distances for paxillin and pFAK are shorter than observed before in REF cells imaged with SIM (Fig. 4E). However, the trend of pFAK cluster showing shorter distances between each other remained the same. For the different FAK constructs, NN distances of FAK dKin, FAK dKin Y397F and mFAT showed slightly lower values, and FAK Y397F and FAK FAT showed slightly higher values compared with FAK wt (FAK dKin, 435 nm; FAK Y397F, 508 nm; FAK dKin Y397F, 425 nm; FAK FAT, 519 nm; mFAT, 462 nm). These differences were not very pronounced, but it is worth mentioning that FAK dKin and FAK dKin Y397F had significantly shorter NN distances compared

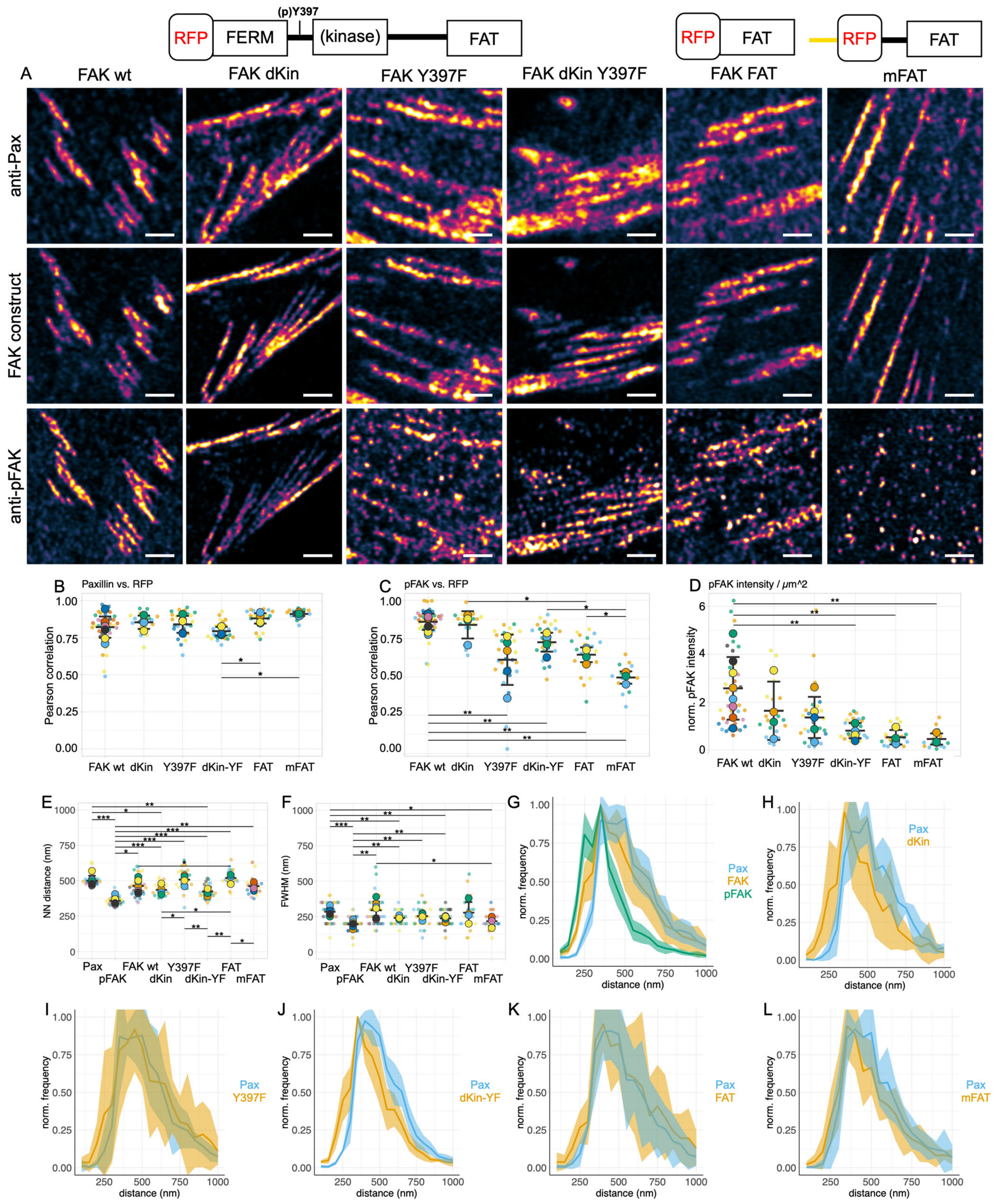

Fig. 5. See next page for legend.

with FAK Y397F (Fig. 5E). Also, of all the FAK constructs, both FAK dKin and FAK dKin Y397F showed a distance distribution that differed the strongest from that of paxillin (Fig. 5H,J). The deletion of the kinase domain in both FAK dKin constructs also abolishes FAK autoinhibition, potentially linking the open FAK conformation to its spatial distribution within

Fig. 5. FAK domains regulate distance distribution of spatial FAK clusters. (A) Schematic diagrams of the constructs used for transfection are shown on top: RFP-tagged FAK full-length constructs, RFP-tagged FAT domain, RFP-tagged FAT domain with membrane anchor (yellow). NIH3T3 cells were transfected with different FAK constructs, fixed, labeled for endogenous paxillin and activated FAK (pFAK), and visualized for anti-Pax immunofluorescence (top panels), RFP-tagged FAK constructs (middle), anti-pFAK immunofluorescence (bottom). Images are representative of four or more experiments. Scale bars: 1 μm. (B,C) Pearson correlation of FAK construct and endogenous paxillin (B) or pFAK (C). Correlation was calculated only for focal adhesion areas identified with paxillin labeling. (D) Fluorescent pFAK intensity per area for the indicated condition. Intensity values were normalized to intensity values of respective FAK constructs to normalize for expression levels. (E–L) NN analysis was used to analyze pFAK and paxillin in FAK wt-transfected cells and all FAK constructs in cells transfected with the respective constructs [*n*=7 (FAK wt, paxillin, pFAK), 5 (FAK dKin Y397F) or 4 (FAK dKin, FAK Y397F, FAK FAT, mFAT); at least 20 cells per condition were analyzed]. NN distance (E) and FWHM analysis (F) from distance distribution plots. (G–L) Histogram based plots (averaged from independent experiments) indicating distance distribution. Significance was tested between all conditions based on independent experiments with Welch's *t*-test after testing for normal distribution with Shapiro–Wilk test. *$0.05 \geq P > 0.01$; **$0.01 \geq P > 0.001$; ***$P \leq 0.001$.

adhesions. Additionally, we plotted distance distributions for all FAK constructs and endogenous paxillin (Fig. 5G–L) as well as FWHM values for paxillin and pFAK labeling from cells expressing FAK wt and all FAK mutants (Fig. 5F). This analysis confirmed that pFAK clusters, like those of pPax-Y118, were closer to each other and showed a more defined spacing compared with labeling of FAK and paxillin.

We also tested whether PIP2-dependent recruitment of FAK to the lipid membrane via the FAK FERM domain could explain the spatial distribution of pFAK clusters. We expressed FAK FERM, a sensor for PIP2 (PLCd PH GFP) or a sensor for phosphatidylinositol-(3,4,5)-trisphosphate (PIP3; sensor AKT PH GFP) in NIH3T3 cells and labeled endogenous paxillin and pFAK (Fig. S5A). AKT PH GFP showed lower Pearson correlation with paxillin and pFAK compared with FAK FERM and PLCd PH GFP (Fig. S5B,C). However, analysis of NN distances (Fig. S5D,E) indicated no differences among the lipid sensors, making it unlikely that the specificity of FAK FERM for PIP2 explains the spatial distribution of pFAK compared with FAK. We also tested constructs for FAK wt, FAK dKin, FAK Y397F and FAK dKin Y397F in mouse fibroblasts with knockout of endogenous FAK (MEF FAK$^{-/-}$). These experiments confirmed the differences observed before for paxillin and FAK wt compared with pFAK (Fig. S5F–H; NN distances for paxillin, 535 nm; FAK wt, 540 nm, pFAK, 363 nm). Among the different FAK constructs (Fig. S5F,H–K), FAK dKin and FAK dKin Y397F again showed the lowest NN distances and mimicked pFAK distribution the most. However, in contrast to experiments in NIH3T3 cells, NN distances for FAK Y397F were shorter than those of FAK wt (FAK dKin, 427 nm; FAK dKin Y397F, 413 nm; FAK Y397F, 451 nm).

Overall, this analysis confirmed that pFAK follows a spatial distribution that is different from paxillin and total FAK; distances between pFAK clusters were shorter and followed a preferred distance for the spacing of pFAK clusters. Mutational analysis indicated that the spatial distribution of FAK could be influenced by its conformational status. In addition, experiments with FAK FERM showed that FAK recruitment to the lipid membrane did not explain the spatial distribution of pFAK. The open conformation of FAK appears to be required for implementing the spatial distribution of pFAK.

Live-cell imaging shows dynamic clusters of FAK

To understand the creation and regulation of spatial clusters in focal adhesions in more detail, we set out to analyze their temporal evolution. First, we cultured REF cells on coverslips and fixed them at different time points after cell seeding, followed by immunolabeling of paxillin and pPax-Y118 (Fig. S6A,B). Starting with culturing cells for 2 h, we observed focal adhesions with the same appearance as described above; paxillin was spread throughout adhesions while pPax-Y118 was confined in distinct spatial clusters. Quantitative analysis with our MATLAB code revealed that the spacing between neighbored pPax-Y118 clusters was preserved over time and remained constant (Fig. S6C). To get more insights into the spatial dynamics of clusters in focal adhesions of living cells, we used NanoJ-SRRF (Gustafsson et al., 2016) and imaged FAK wt, FAK dKin, mFAT and paxillin (Fig. 6). We imaged living NIH3T3 cells expressing these proteins on a total internal reflection fluorescence (TIRF) microscope and calculated super-resolution radial fluctuation (SRRF) images (25 images taken at 20 Hz used for one SRRF image, temporal resolution 1.25 s/SRRF frame). According to NanoJ SQUIRREL (Culley et al., 2018), we achieved a local resolution with these settings of around 100 nm and lower (Fig. 6A″). Analyzing single adhesions from these movies with kymographs indicated spatial clusters for all FAK constructs, but also identified different mobility behaviors (Fig. 6B). While FAK wt clusters showed dynamic cluster movements, including merging and splitting, mFAT clusters appeared more stable. Paxillin, in contrast, showed a lower tendency to cluster and was more spread throughout adhesions. Kymographs of FAK dKin showed long-lasting tracks, similar to mFAT. In contrast to all FAK constructs, tracks of paxillin were harder to identify, potentially reflecting the broader distribution of paxillin in distance distribution plots (Fig. 2B). We calculated mean square displacement (MSD) values based on tracks of clusters to describe dynamic behavior (Fig. 6D). We also imaged fixed cells expressing FAK wt and calculated MSD values as a reference for immobile tracks. This information was used to define a mobile fraction in living cells and to calculate corresponding MSD values (Fig. 6E). All MSD values (FAK wt, 0.00675 μm^2/s; FAK dKin, 0.00752 μm^2/s; mFAT, 0.00376 μm^2/s; paxillin, 0.0042 μm^2/s) were in a similar range to earlier reports of nanoclusters of $\alpha L\beta 2$ integrin binding to ICAM-1 (0.0078 μm^2/s, Diez-Ahedo et al., 2009). Overall, FAK wt and FAK dKin showed the highest MSDs, however, with more variation in the case of FAK wt. Additionally, we calculated cross-correlation values between every fifth temporal frame (Fig. 6C). Based on this calculation, high cross-correlation indicated little spatial change within five timeframes (5×1.25 s) and vice versa. FAK wt showed low cross-correlation corroborating higher mobility of clusters compared to all other conditions (Fig. 6F). Thus, cross-correlation and MSD values both indicate higher dynamics of FAK wt clusters. The FAK mutant in a constitutively open conformation, FAK dKin, showed similar MSD but less abrupt changes judging from cross-correlation values. Paxillin and mFAT both showed reduced mobility compared with that of FAK dKin.

Super-resolution live-cell imaging with SRRF confirmed the presence of spatial clusters of FAK constructs within focal adhesions. Moreover, it became clear that the spatial dynamics of these clusters differ between paxillin and FAK, showing higher dynamics for the latter. Reduced dynamics of mFAT might reflect its binding to the more stable paxillin, and also the lack of kinase activity of FAK and/or of Src.

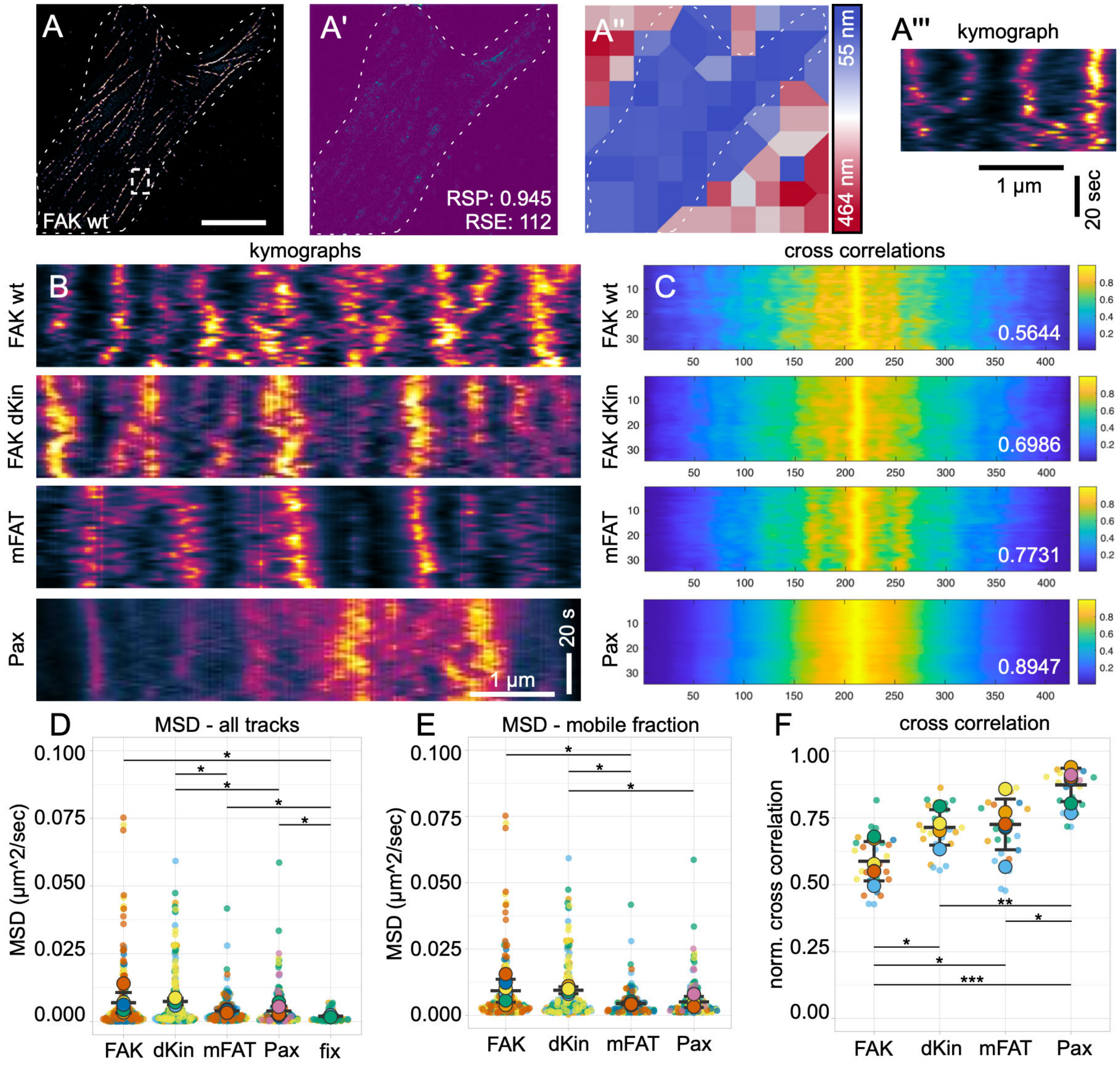

Fig. 6. Live-cell imaging with TIRF and SRRF highlights dynamics of spatial FAK and Pax clusters. (A,B) NIH3T3 cells were transfected with the indicated constructs and imaged with TIRF microscopy (25 frames for one SRRF image, one final frame per 1.25 s). (A–A‴) NanoJ-SQUIRREL: error maps [resolution-scaled Pearson coefficient (RSP) and resolution-scaled error (RSE)] (A′) and maps of local resolution (colors indicate resolution as shown in the blue–red color bar; darkest blue, 55 nm; darkest red, 464 nm) (A″). Areas containing focal adhesions resolved around 100 nm (indicated in blue). White dashed lines indicate the cell outline, white dashed box in A indicates the region used for the kymograph in A‴. Scale bars: 1 µm (horizontal), 20 s (vertical). (B) Kymographs of single adhesions covering 50 s were isolated from SRRF movies. Scale bars: A, 10 µm; A‴, 1 µm (horizontal), 20 s (vertical). (C) Cross-correlation was calculated between every fifth consecutive time frame and plotted for kymographs shown in B after normalization to the highest value for each kymograph; normalized cross-correlation according to the color bar; *y*-axis indicates the time in seconds, *x*-axis indicates the relative spatial value in pixels. Values indicate average of normalized cross-correlation plots shown here. (D) MSD values were calculated based on tracks in kymographs as shown in Fig. 6B [3–4 cells from three independent experiments, more than 20 kymographs analyzed (except for fixed cells, 8 kymographs analyzed); small points represent individual MSD values, big dots represent average per cell]. (E) MSD values only of mobile tracks. Mobile tracks as a percentage of total tracks: FAK wt, 77%; FAK dKin, 76%; mFAT, 83%; paxillin, 75%. In D,E, every small dot indicates a single track in a kymograph, big dots indicate the average per cell from three independent experiments. (F) Average cross-correlation values for each kymograph. Significance was tested between all conditions based on single cells with Welch's *t*-test after testing for normal distribution with Shapiro–Wilk test (F) or (with Mann–Whitney-*U*-test due to non-normal distribution of MSD values (D,E). $^{*}0.05 \geq P > 0.01$; $^{**}0.01 \geq P > 0.001$; $^{***}P \leq 0.001$.

Spacing of pPax clusters is mechanosensitive and depends on vinculin

Finally, we wondered whether it is possible to interfere with the spacing between clusters of phosphorylated proteins depending on cell contractility. Previous publications have indicated that actomyosin contractility increases paxillin phosphorylation (Pasapera et al., 2010; Zaidel-Bar et al., 2007). At the same time, several reports highlighted a force-dependent activity of FAK (Bauer et al., 2019; Torsoni et al., 2003; Wong et al., 2011). Thus, we treated REF cells with the myosin inhibitor blebbistatin or with Y27632 (Rho-ROCK pathway inhibitor) and labeled paxillin and pPax-Y31 (Fig. 7A–C; pPax-Y31 showed no differences from pPax-Y118; Fig. S2C,D). Analysis with our MATLAB workflow indicated a reduction in pPax-Y31 cluster spacing (Fig. 7D) and of pPax-31 localization in adhesions (Fig. 7E) for both inhibitors. Thus, reduced contractility caused a higher density of pPax clusters within focal adhesions but a reduction in the total amount of pPax-Y31.

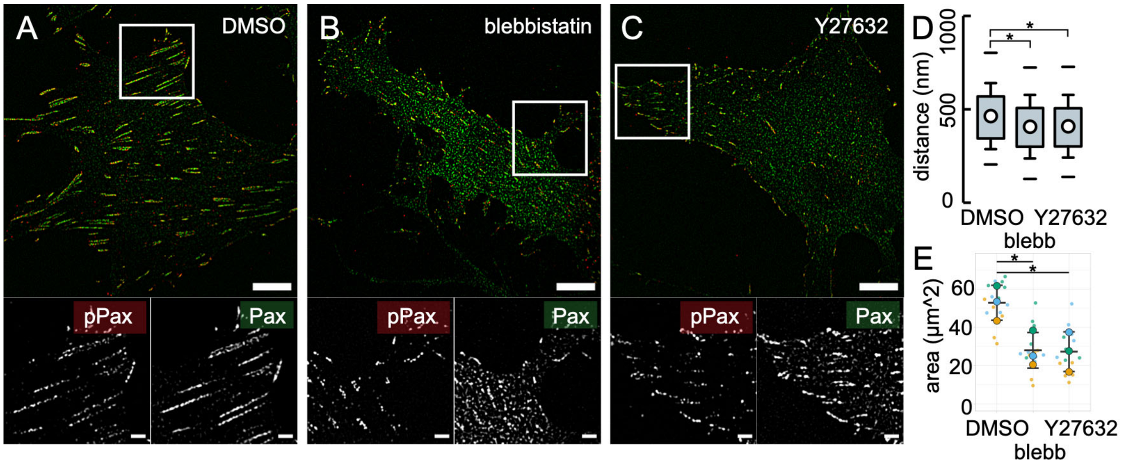

Fig. 7. pPax-Y118 cluster distance is mechanosensitive. (A–C) REF cells cultured for 6 h and (when indicated) incubated with 20 µm blebbistatin (blebb) or Y27632 for the last hour of experiment. Cells were fixed and labeled for paxillin and pPax-Y31. Magnified images of the white boxes in overviews show pPax-Y31 or paxillin as indicated. Images are representative of three experiments. Scale bars: 10 µm in overview and 2 µm in magnified images. (D) Quantitative analysis of pPax-Y31 cluster distance (MATLAB workflow; *n*=3, at least 15 cells per condition). (E) Analysis of pPax-Y31 area per cell. Significance was tested between all conditions based on independent experiments with Welch's *t*-test after testing for normal distribution with Shapiro–Wilk test. *0.05≥*P*>0.01.

Paxillin phosphorylation has also been linked to vinculin recruitment (Pasapera et al., 2010). To test this, we cultured mouse embryonic fibroblasts from vinculin knockout mice (MEF Vin$^{-/-}$) and analyzed pPax-Y118 in these cells compared with MEF wt cells (Fig. 8). Quantitative analysis of the pPax-Y118 cluster distance revealed an increase in the cluster distance in the absence of vinculin (Fig. 8E). Additionally, we tested the impact of cellular contractility in MEF cells (Fig. 8C,D) as done before in REF cells. These experiments confirmed that reduced cellular contractility decreases pPax-Y118 spacing (Fig. 8E) as observed before for pPax-Y31 in REF cells.

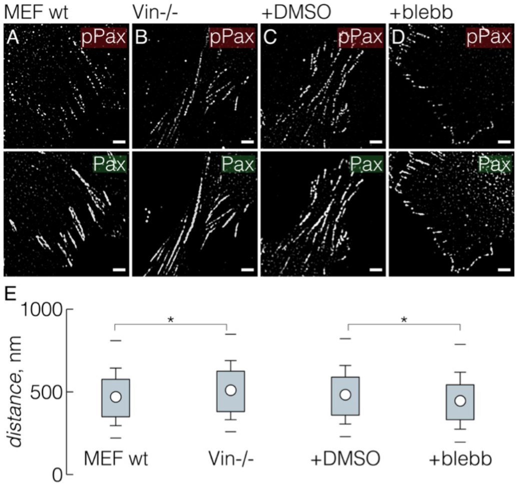

Fig. 8. Cell contractility and vinculin expression modify the distance of pPax-Y118 clusters. (A) MEF wt cells cultured on coverslips and labeled for paxillin (green) and pPax-Y118 (red). (B) MEF cells from vinculin knockout mice (Vin$^{-/-}$) were treated as described in A. (C–D) MEF wt cells were treated as described in A but treated with DMSO or blebbistatin (blebb, 20 µM) for the last hour of the experiment when indicated. Images are representative of three experiments. Scale bars: 2 µm. (E) Quantification of pPax-Y118 cluster distance for cells described in A–D (*n*=3, at least 24 cells were analyzed per condition). Significance was tested between MEF wt and MEF Vin$^{-/-}$ cells and between MEFs treated with DMSO or blebbistatin based on independent experiments with Welch's *t*-test after testing for normal distribution with Shapiro–Wilk test. *0.05≥*P*>0.01.

To conclude, actomyosin contractility affected the spacing of pPax clusters within focal adhesions in REF cells and in MEF wt cells. Moreover, we showed that vinculin expression impacted pPax-Y118 cluster spacing.

DISCUSSION

We set out to study whether adhesome proteins show different lateral organization within integrin-mediated adhesions. We observed that several adhesome proteins appeared to localize homogenously in focal adhesions when observed with SIM. This observation was in striking contrast to pPax and pFAK localization, for which we detected clusters that were spatially separated from each other using super-resolution light microscopy. Additionally, we found that these clusters have a more defined spacing between them compared with the intensity maxima of labeling for paxillin and FAK. Control experiments and quantifications confirmed this impression irrespective of the antibodies used and for different microscopic methods. However, STED imaging at higher resolution indicated that protein localization is not binary and that a minority of pFAK can also localize outside of these clusters. Live-cell imaging of different FAK constructs and paxillin indicated that all FAK constructs had a tendency to localize in clusters compared with paxillin. Finally, experiments with contractility inhibitors pointed to a connection of the distribution of pPax clusters to actin-mediated forces on adhesions.

Focal adhesions have been a popular target of super-resolution microscopy from the beginning of the development of these techniques (Betzig et al., 2006). The work by Betzig and colleagues already demonstrated that vinculin is organized with fluctuating density in focal adhesions, creating more and less dense areas of vinculin. Since these earliest super-resolution reports, the pointillistic nature of focal adhesions has been confirmed many times when observed with high resolution microscopy (Bachmann et al., 2016; Changede et al., 2015; Diez-Ahedo et al., 2009; Shroff et al., 2008, 2007; Spiess et al., 2018; Xu et al., 2018). In the work presented here, we mostly used super-resolution methods that have limited resolution (typically around 100 nm) compared with the studies mentioned before. These reports using higher resolution methods found diameters of spatially confined clusters of integrins within focal adhesions to be in a range from 40 nm (Shroff et al., 2008; Spiess et al., 2018) to 100 nm (Changede et al., 2015). At the same time, cryo-electron microscopy showed even smaller structures at adhesion sites (Patla et al., 2010; donut-shaped structures connected to actin with a diameter around 20 nm and nearest neighbor distance of 15–60 nm). In fact, our STED images at higher resolution (15% depletion laser, resolution around 68 nm) also indicated substructures within some clusters that were not resolved at low resolution (Fig. S4D; for example, first maxima 0% versus 5% depletion laser). Moreover, higher-resolution imaging also revealed some pFAK labels that were not detected at lower resolution (arrow in Fig. S4A,D). These dim pFAK species imply that the spatial distribution of pFAK (and most likely other phosphorylated adhesome proteins) is not binary as it appeared from SIM images. A non-binary spatial organization is also in line with reports showing clusters of different adhesome proteins throughout adhesions (Bachmann et al., 2016; Changede et al., 2015; Diez-Ahedo et al., 2009; Shroff et al., 2007, 2008; Spiess et al., 2018; Xu et al., 2018). However, it appears that such dim pFAK species account for a minority of labeled protein. Thus, the spatial organization of adhesome phosphoproteins might be preferentially, but not exclusively, in clusters. Such a preferred localization of phosphoproteins in ‘hotspots’ or functional clusters has also been described by Ballestrem and colleagues using Förster resonance energy transfer (FRET) (Ballestrem et al., 2006). Importantly, the clusters we described here are well above the resolution limit, even of conventional microscopy (Fig. 2E, diameter of Pax-Y118 clusters around 267 nm). In fact, published images of pPax or pFAK already show ‘pointy’ or ‘spotty’ localization (see, for example, Horton et al., 2016; Pasapera et al., 2010; Zaidel-Bar et al., 2007). These arguments further strengthen the point for the existence of pPax and pFAK clusters.

The question remains how these differences in spatial distribution between pFAK and pPax, on the one hand, and FAK and paxillin, on the other hand, are implemented on the molecular level, and why they are organized in this particular manner. FAK is recruited to the lipid membrane and focal adhesions in an inactive closed conformation before auto-phosphorylation of Y397 activates FAK by releasing the kinase domain from inhibitory binding to FAK FERM. Thus, the distance distributions of FAK and pFAK indicate differences in the spatial distribution of the conformations of FAK, i.e. an equilibrium of FAK conformations in the case of FAK, versus only the open FAK conformation in the case of pFAK. Of the FAK constructs we tested, FAK Y397F can be considered to be locked in a closed conformation. At the same time, the constructs FAK dKin and FAK dKin Y397F that lack the kinase domain can be considered to be locked in an open conformation. Indeed, NN distances of both FAK dKin and FAK dKin Y397F were significantly shorter (and thereby closer to that of pFAK) compared with NN distances of FAK Y397F (Fig. 5E). Thus, an open FAK conformation might be needed to achieve the particular spatial distance distribution observed for pFAK. Studies in FAK$^{-/-}$ cells (Fig. S5F–K) also showed shorter distances for FAK constructs lacking a kinase domain compared with FAK wt. However, NN distances of FAK Y397F were similar to both FAK dKin constructs and differed in this regard from experiments in the presence of endogenous FAK. An additional contributing factor for the spatial distribution of pFAK could be the binding of Src to the active FAK complex. In this regard, it is noteworthy that FAK dKin has a phosphorylated Src-binding site that is lost in FAK dKin Y397F due to the additional Y397F mutation. Nevertheless, both mutations show similar NN distances and a similar distance distribution implying that Src binding is not essential for the spatial distribution of pFAK.

Live-cell imaging of different FAK constructs and of paxillin (Fig. 6) showed clustered localization of all FAK constructs but a less clustered distribution of paxillin. This difference indicates that distance distributions of FAK wt and pFAK do not differ because of an inability of FAK wt to cluster, but rather because of an inability to keep a defined distance between clusters. Indeed, tracks of FAK wt (Fig. 6B) showed abrupt changes while FAK dKin clusters followed more consistent tracks. This difference could be related to FAK dKin being locked in an open conformation compared with FAK wt undergoing conformational changes. Tracks of mFAT appeared to be more clustered than was the case for paxillin. This was surprising for us, given that mFAT localizes to adhesions only via FAT, the paxillin-binding domain of FAK. Thus, clustering of FAK constructs might be linked to FAK–paxillin binding via the FAT domain. At the same time, there are many reports highlighting the relevance of FAT–paxillin binding for FAK localization in adhesions and for FAK activity (Deramaudt et al., 2011, 2014; Mousson et al., 2021). This motivated us to study in more detail how FAK and paxillin interact. FAK FAT is reported to bind paxillin via its LD2 and LD4 motifs (Hoellerer et al., 2003). At the same time, several reports point to the relevance of paxillin phosphorylation at Y31 and Y118 for paxillin–FAK interaction (Choi et al., 2011; Digman et al., 2009). However, Y31 and Y118 are clearly located outside of the LD2/LD4 domains, raising the question of how pY31 and pY118 are supposed to impact FAT–paxillin binding. No protein structure of full-length paxillin is currently available and, therefore, we studied AlphaFold (Jumper et al., 2021; Mirdita et al., 2021preprint) predictions of paxillin (Fig. S7). All five predictions of paxillin suggested that paxillin LIM domains are organized as a rigid rod while N-terminal LD domains and unstructured regions are flexible with no clear spatial arrangement between the different domains (Fig. S7A,C). The only two exceptions are two models (confidence rank 1 and rank 3) where Y31 and Y118 localize on the surface of LIM domains in areas with negative surface charges (Fig. S7B–E). Importantly, these models show the lowest error for the spatial arrangement between Y31/Y118 and LIM domains (Fig. S7D), indicating that these models are more likely compared with models where Y31/Y118 do not bind LIM domains. Binding of Y31/Y118 on the LIM surface will lead to LD motifs being wrapped around the LIM rod (Fig. S7A), thereby limiting steric access of FAK FAT to paxillin LD2 and LD4 motifs. However, phosphorylation of Y31 and Y118 will cause electrostatic repulsion to the negative surface of LIM domains. This will free not only Y31/Y118 but also LD motifs, release steric constraints, and eventually allow FAT–LD2/LD4 binding. In this scenario, FAT binding to phosphorylated paxillin will bring the FAK–Src complex in close proximity to paxillin. The FAK–Src complex is able to phosphorylate paxillin Y31 and Y118, in turn stabilizing FAK–paxillin interaction. Eventually, this establishes a positive feedback loop that can spawn local clusters of pFAK and pPax and explain their similar spatial distributions that we observed here. Such a positive feedback loop could be limited by FAK switching back to its closed conformation (dephosphorylation of pY379) and/or by reducing the FAT–paxillin interaction that affects FAK recruitment to adhesions and signaling (Deramaudt et al., 2011, 2014; Mousson et al., 2021). In this respect, a phosphorylation site in FAK FAT (Y925) was shown to prevent paxillin binding when phosphorylated by Src (Kadaré et al., 2015). Thus, FAK–Src binding could be part of the positive feedback loop described above, while, at the same time, it could apply a limit to the progression of the feedback loop.

Several reports showed that FAK activation and kinase activity is increased by mechanical forces (Bauer et al., 2019; Seong et al., 2013; Torsoni et al., 2003; Wong et al., 2011) and that contractility inhibition decreases paxillin phosphorylation at Y31/Y118 (Fig. 7E, (Zaidel-Bar et al., 2007)) and also FAK phosphorylation at Y397 (Pasapera et al., 2010). The fact that both FAK-Y397 phosphorylation and paxillin phosphorylation depend in the same manner on contractility is in line with the hypothesis of a positive feedback mechanism between these two events. For clusters of pPax, we found in two different cell lines that contractility reduction causes a small but significant reduction in cluster spacing. Thus, reduced pPax levels are connected to reduced spacing of pPax clusters, suggesting that less pPax leads to a shorter distancing between neighbored pPax clusters. This finding fits a model of lateral inhibition in which the local amount of pPax reduces at the same time as does the concentration of pPax in its vicinity. It will be interesting to test in more detail whether this effect indicates a patterning mechanism according to Turing (reviewed in Howard et al., 2011) for pPax spacing. Such a model is not mutually exclusive with a role of paxillin LIM domains in sensing actin fibers under mechanical stress (Sun et al., 2020; Winkelman et al., 2020) and/or sensing their contractility-dependent angle towards adhesions and the lipid membrane (Liu et al., 2015).

Vinculin knockout caused a small increase in pPax spacing compared with that in wild-type cells. Vinculin knockout leads to reduced traction stress (Thievessen et al., 2013), probably linked to the function of vinculin as a mechanical talin-actin linker (Carisey et al., 2013; Grashoff et al., 2010; Humphries et al., 2007). Based on these findings, we expected that vinculin knockout phenocopies contractility inhibition. Instead, we found the opposite. A possible explanation for this contradiction could be that the relevance of vinculin for mechanical force transmission, on the one hand, and for paxillin binding, on the other, cause opposing effects for pPax cluster spacing that require further analysis.

We also wondered about the evolutionary advantage of clustering pFAK/pPax in adhesions. It might be interesting to consider alternative spatial organizations: Why are pPax/pFAK not spread more homogenously throughout focal adhesions? One possibility might be that pPax/pFAK signals have to be detected in the noisy environment of protein phosphorylation. In this case, it might be advantageous to locally concentrate a pPax/pFAK signal so that it may exceed the background noise; this would not be the case if pPax/pFAK were homogenously spread in focal adhesions. A mechanism of local enrichment to increase signal strength is, to our knowledge, hypothetical for focal adhesions. However, the general idea of local signal enhancement by concentrating the signal also applies to other cell signaling events. Lipid rafts concentrate transmembrane proteins, myelinated axons organize localized depolarization at myelin-sheath gaps, and filopodia concentrate signaling pathways in a limited volume compared to the complete cell body. Thus, it might not be surprising if signaling hubs like focal adhesions also implement the same strategy.

In summary, we have presented new data for the structural implementation of paxillin and FAK and their phosphorylated forms in focal adhesions. pPax and pFAK preferentially localize in clusters with a distance distribution that differs from that of paxillin and FAK that are organized more randomly. This suggests a regulated spacing mechanism for such pPax/pFAK signaling hubs, thereby connecting the function of focal adhesions with their lateral structure. Mutational analyses of FAK point to the open conformation of FAK to be necessary for the regularity of pFAK cluster spacing, whereas paxillin–FAT binding appears to regulate FAK clustering itself. Further work will address the dynamics of the FAK–paxillin interaction in more detail and the connection of FAK clusters to other components of the adhesome.

MATERIALS AND METHODS

Cell culture and plasmids

Cells were cultured in Dulbecco's Modified Eagle Medium (DMEM, Pan-Biotech, Germany) supplemented with 10% fetal calf serum (FCS, HyClone, USA) at 5% CO_2 and 37°C. NIH3T3 cells, HeLa cells and NRK cells were obtained from American Type Culture Collection (ATCC, USA). Rat embryonic fibroblasts were a gift from B. Geiger and human foreskin fibroblasts (HFFs) were obtained from PromoCell (Germany). MEF wt cells and MEFs from vinculin knockout mice (MEF Vin$^{-/-}$) were a gift from W.H. Ziegler (Mierke et al., 2010). MEFs from FAK knockout mice (MEF FAK$^{-/-}$) were a gift from S. Aizawa (Ilić et al., 1995) and P. Rondé. Transfections were carried out with Lipofectamine 2000 (ThermoFisher) according to the manufacturer's instructions. cDNA encoding the full-length mouse β3-wt–GFP integrin expressed in a cytomegalovirus promoter-driven pcDNA3/EGFP vector has been previously described (Ballestrem et al., 2001), zyxin–RFP was deposited by A. Huttenlocher (Addgene #26720; Bhatt et al., 2002) and vinculin wt GFP was a gift from C. Ballestrem (Humphries et al., 2007). Paxillin–GFP was prepared as described before (Ripamonti et al., 2021), as well as PLCd PH GFP (Saltel et al., 2009), AKT PH GFP (Ivarsson et al., 2013) and talin1–GFP (Saltel et al., 2009). The coding sequence for mouse FAK was a gift from David Schlaepfer (UCSD, USA). Fluorophores were exchanged to tagRFP and mutations were introduced with site-directed mutagenesis followed by digestion and ligation using unique restriction sites. FAK dKin Y397F was created by ClaI+XbaI digestion of FAK dKin and FAK Y397F, followed by replacement of the kinase-containing part of FAK Y397F with the kinase-deleted part from FAK dKin. mFAT was created by replacing FAK FERM and the kinase domain from tagRFP FAK wt with Lck-mScarletI (deposited by Dorus Gadella; Addgene #98821; Chertkova et al., 2020preprint) by NheI and XhoI digestion and ligation. FAK sequence in mFAT starts with Ser840.

Antibodies and reagents

Inhibition experiments were performed with blebbistatin (Sigma-Aldrich, USA) or with the ROCK inhibitor Y27632 (Sigma-Aldrich, USA) at concentrations as indicated. Immunostaining was performed after fixation of cells with 4% paraformaldehyde (Sigma-Aldrich, USA) in PBS. Reagents used for immunostaining were mouse antibodies against paxillin (BD Biosciences, #610051, 1:500 or 1:100, 1:500, 1:1000, 1:5000 in Fig. S2E-H) and vinculin (Sigma-Aldrich, #V-9131, 1:100), rat antibodies against α5 integrin (BMB5 clone, Merck, #MAB2514, 1:100) and rabbit antibodies against pPax-Y118 (Cell Signaling, #2541S, 1:500 or 1:100, 1:500, 1:1000 for Fig. S3: ThermoFisher, #44722G, 1:100, 1:500, 1:1000 for Fig. S3), against pPax-Y31 (ThermoFisher, #44720G, 1:100, 1:500, 1:1000 for Fig. S3 and 1:500 for Fig. 7), against pTyr (Sigma-Aldrich, #T1325, 1:500) and against pFAK-Y397 (ThermoFisher, #700255, 1:1000). Primary antibody staining was followed by washing steps and incubation with antibodies against mouse antibodies labeled with Cy3 (Jackson Immunoresearch, #115-165-146, 1:500), against rabbit antibodies labeled with Alexa Fluor 488 (ThermoFisher, #A11070, 1:500) or Cy3 (1:500, Dianova, #111-165-144, 1:500), or with phalloidin coupled to Alexa Fluor 647 (1:200, ThermoFisher, #A22287). Primary rat antibodies were visualized with Alexa Fluor 488-labeled secondary antibodies (ThermoFisher, #A11006, 1:500).

Microscopy

SIM imaging was performed on a non-serial Zeiss Elyra PS.1 microscope with a 63×/1.4NA oil immersion objective and an Andor iXon EMCCD camera. The grid for SIM was rotated three times and shifted five times leading to 15 frames of raw data, out of which a final SIM image was calculated with the structured illumination package of ZEN software (Zeiss). Values for calculation were selected for best resolution without causing image artifacts. Channels were aligned using a correction file that was generated by measuring channel misalignment of fluorescent tetraspecs

(ThermoFisher, #T7280). Airyscan imaging was performed on a Zeiss LSM 800 with a 63×/1.4NA oil immersion objective and in super-resolution AiryScan mode. Data for NanoJ-SRRF (Gustafsson et al., 2016) were acquired in TIRF mode on a Nikon Eclipse Ti with perfect focus system, 100×/1.49 NA oil objective and an Andor-EMCCD iXon897 camera. STED images were acquired on a Leica TCS SP8 STED 3× in gated STED mode and with Lightning deconvolution. Images were acquired with a 100×/1.4NA oil immersion objective. Depletion laser intensity and pixel size are indicated in the text. Secondary immunolabeling of pFAK was done with anti-rabbit Abberior Star Red (abberior, #STRED-1002-500UG, 1:1000). Live cell imaging was performed on a heated stage at 37°C and 5% CO_2. Cells were cultured on fibronectin-coated (10 µg/ml, 1 h at room temperature) glass-bottom dishes in DMEM+10% FCS for 5 h. Medium was changed to F12 buffer (ThermoFisher, USA) with 1% FCS 1 h before imaging. Cells were imaged for 2–3 min with 50 ms framerate. NanoJ-SRRF was used to calculate super-resolution frames consisting of 25 raw frames, i.e. 1 SRRF frame/1.25 s. Quality and resolution of SRRF movies was analyzed with NanoJ-SQUIRREL (Culley et al., 2018).

Image analysis

Images were prepared and analyzed (intensity profiles) using the Fiji software package (Schindelin et al., 2015). Line profiles were measured by averaging over the width of single adhesions in order to consider the full width of focal adhesion stripes. For analysis of spot-to-spot distance, we used a custom-written software, utilizing MATLAB Image Processing Toolbox (The MathWorks Inc., USA) and a nearest neighbor method in ImageJ (see below). The workflow for MATLAB-based process was as follows: two images, one serving as a focal adhesion mask and one being the staining of interest, were needed. Labeled paxillin or vinculin was used as mask in our case (Fig. S1A, Mask) while pPax, pFAK or pTyr were labels of interest (Fig. S1A, Image of interest). The mask image was thresholded and structures below an area limit of 1–3 μm^2 were excluded in order to limit the analysis to focal adhesions. Optionally, focal adhesions within a mask could be slightly broadened by adding the desired number of pixels (typically around one) around their periphery to ensure them covering most of the labels of interest within focal adhesions. Then, all focal adhesions within the mask were indexed and fitted as ellipses to extract their positions, lengths and widths (Fig. S1A, Characterize). Based on these features, labeled areas within corresponding focal adhesions were isolated and an intensity line profile was created for a peak-to-peak distance calculation (Fig. S1A, Intensity profile). Size of individual spots was also extracted from intensity line profiles as width of each peak at its half prominence. Images were pre-processed in similar ways for nearest neighbor analysis and for measuring correlation and co-occurrence: the paxillin channel was background subtracted (sliding paraboloid, rolling ball radius: 1 pixel); mask for focal adhesions was created (threshold Otsu, create selection, enlarge selection −0.1 µm followed by +0.1 µm to remove structures smaller than focal adhesions); this selection was transferred to unprocessed images of labeled proteins of interest to be analyzed. Measurements of nearest neighbor distances were performed with the ImageJ plugin NanoJ-Core (Laine et al., 2019). Tolerance levels were chosen in order to faithfully detect peaks of intensity (SIM images, 1000; AiryScan, 100). Distance values (>100 nm and <1000 nm) obtained either with the NN method in NanoJ-Core or with our MATLAB workflow were used to create histograms with a bin width of 50 nm. For FWHM analysis, we counted the number of bins with normalized frequency $\geq$0.5 and multiplied this number with 50 nm as a measure for FWHM. FWHM plots show these values as small dots and averages per independent replicate as big dots. For distance distribution plots, measured distances were pooled for one independent experiment and histograms were created per independent experiment. These histogram data were used to plot distance distribution with PlotTwist (Goedhart, 2020). Correlation and co-occurrence were calculated with the ImageJ plugin JACoP (Bolte and Cordelieres, 2006). Correlation between pFAK and lipid sensors was calculated after using masks based on pFAK staining, not paxillin staining. Kymographs were created, tracks identified and analyzed (MSD) with the plugin KymographTracker (version 1.1.0.0; Chenouard et al., 2010) in Icy (de Chaumont et al., 2012). Cross-correlation of kymographs was calculated with a custom-written MATLAB code. We calculated the average normalized cross-correlation between every fifth-time slice (i.e. first slice in cross-correlation plot=cross-correlation of first and fifth slice in kymograph; second slice cross-correlation=cross-correlation of second and sixth slice in kymograph, and so on). This approach was chosen because changes between consecutive slices was high for all conditions, masking dynamic changes occurring over more than one time frame (=1.25 s). The scale of normalized cross-correlation is 0 to 1, where 1 indicates perfect correlation and, therefore, spatial consistency across the intensities during the observed time period. *x*-axis in cross-correlation plots is a relative spatial value and does not directly correlate to *x*-values in kymographs.

Statistics and software

In Figs 3,7,8, Figs S2, S6, data in box plots are represented as follows: dot within the box representing mean value, box outline representing the 25th and 75th percentiles, whiskers representing standard deviation, and upper and lower bars representing the 5th and 95th percentiles. Preparation of graphs and statistical significance testing were done with OriginPro 2017 software (OriginLab Corp., USA). In Figs 2–7, Figs S3–S5, figures were prepared with PlotTwist (Goedhart, 2020) for histogram-based distance distribution plots and SuperPlotsOfData (Goedhart, 2021) for bar charts. Distance distribution plots show mean (indicated as thick line) and 95% confidence intervals (shade) calculated from independent experiments. Bar charts show technical replicates as small dots and mean from independent experiments as big dots. Black lines indicate mean from all independent experiments and upper and lower black line show standard deviation. The numbers of independent experiments are mentioned in figure legend as ‘*n*’. Statistical tests were performed by SuperPlotsOfData and PlotTwist, respectively. When tests for normal distribution (Shapiro–Wilk test) indicated non-normal distribution for the majority of conditions (applied to Fig. 6D,E), we calculated Mann–Whitney *U*-test instead (Jupyter notebook implemented code, stats package from scipy; code available, see Data availability section) Paxillin models were created with AlphaFold (Jumper et al., 2021) and ColabFold (Mirdita et al., 2021 preprint); MSA alignment was performed with Jackhmmer. Visualization of models of paxillin structure was done in Chimera X (Goddard et al., 2018; Pettersen et al., 2021).

Acknowledgements

We are grateful to Monica Julio Barreto and Tatiana Fomekong for help with molecular cloning and to Nikolaos Athanasopoulos and Christopher Henry for their help with data analysis. We thank the bioimaging core facility of University of Geneva for their help and support and Philippe Rondé (Université de Strasbourg, France) for help with reagents. We acknowledge UCSF ChimeraX, developed by the Resource for Biocomputing, Visualization, and Informatics at the University of California, San Francisco, with support from National Institutes of Health (R01-GM129325) and the Office of Cyber Infrastructure and Computational Biology, National Institute of Allergy and Infectious Diseases.

Competing interests

The authors declare no competing or financial interests.

Author contributions

Conceptualization: M. Bachmann, A.S., B.W.-H., M. Bastmeyer; Methodology: A.S., M. Bachmann; Software: A.S.; Formal analysis: M. Bachmann, A.S.; Resources: A.S., B.W.-H., M. Bastmeyer; Data curation: M. Bachmann, A.S., K.W.; Writing - original draft: M. Bachmann, A.S.; Writing - review & editing: M. Bachmann, A.S., B.W.-H., M. Bastmeyer; Visualization: M. Bachmann, A.S.; Supervision: M. Bachmann, B.W.-H., M. Bastmeyer; Project administration: M. Bachmann, M. Bastmeyer; Funding acquisition: M. Bastmeyer, B.W.-H.

Funding

M. Bachmann acknowledges funding by Deutsche Forschungsgemeinschaft (DFG, German Research Foundation; BA 6471/1-1). A.S. acknowledges funding from the Erasmus Mundus Europhotonics program. The work of M. Bastmeyer is supported by the Deutsche Forschungsgemeinschaft under Die Exzellenzstrategie des Bundes und der Länder (Germany’s Excellence Strategy) through EXC 2082/1-390761711 (3DMM2O Excellence Cluster by the Karlsruhe Institute of Technology and Heidelberg University). The work of B.W.-H. is supported by the Schweizerischer Nationalfonds zur Förderung der Wissenschaftlichen Forschung (Swiss National Science Foundation, grant 310030_185261 and 310030L_170112).

Data availability

Microscopy images analyzed for this study, analyzed data, MATLAB code and ImageJ macro codes are accessible on Yareta (the archive portal of University of Geneva) at doi:10.26037/yareta:lapi22rvsfddrgtmip4ffi4p2i. All code is accessible via Github (https://github.com/Mitchzw/pPax-and-pFAK-in-adhesions).

Peer review history

The peer review history is available online at https://journals.biologists.com/jcs/article-lookup/doi/10.1242/jcs.258764.

References

Aaron, J. S., Taylor, A. B. and Chew, T.-L. (2018). Image co-localization - co-occurrence versus correlation. *J. Cell Sci.* **131**, jcs211847. doi:10.1242/jcs.211847

Acebrón, I., Righetto, R. D., Schoenherr, C., de Buhr, S., Redondo, P., Culley, J., Rodriguez, C. F., Daday, C., Biyani, N., Llorca, O. et al. (2020). Structural basis of Focal Adhesion Kinase activation on lipid membranes. *EMBO J.* **39**, e104743. doi:10.15252/embj.2020104743

Arold, S. T. (2011). How focal adhesion kinase achieves regulation by linking ligand binding, localization and action. *Curr. Opin. Struct. Biol.* **21**, 808-813. doi:10.1016/j.sbi.2011.09.008

Arold, S. T., Ulmer, T. S., Mulhern, T. D., Werner, J. M., Ladbury, J. E., Campbell, I. D. and Noble, M. E. M. (2001). The role of the Src homology 3-Src homology 2 interface in the regulation of Src kinases. *J. Biol. Chem.* **276**, 17199-17205. doi:10.1074/jbc.M011185200

Bachmann, M., Fiederling, F. and Bastmeyer, M. (2016). Practical limitations of superresolution imaging due to conventional sample preparation revealed by a direct comparison of CLSM, SIM and dSTORM. *J. Microsc.* **262**, 306-315. doi:10.1111/jmi.12365

Bachmann, M., Kukkurainen, S., Hytönen, V. P. and Wehrle-Haller, B. (2019). Cell Adhesion by Integrins. *Physiol. Rev.* **99**, 1655-1699. doi:10.1152/physrev.00036.2018

Ballestrem, C., Hinz, B., Imhof, B. A. and Wehrle-Haller, B. (2001). Marching at the front and dragging behind: differential alphaVbeta3-integrin turnover regulates focal adhesion behavior. *J. Cell Biol.* **155**, 1319-1332. doi:10.1083/jcb.200107107

Ballestrem, C., Erez, N., Kirchner, J., Kam, Z., Bershadsky, A. and Geiger, B. (2006). Molecular mapping of tyrosine-phosphorylated proteins in focal adhesions using fluorescence resonance energy transfer. *J. Cell Sci.* **119**, 866-875. doi:10.1242/jcs.02794

Bauer, M. S., Baumann, F., Daday, C., Redondo, P., Durner, E., Jobst, M. A., Milles, L. F., Mercadante, D., Pippig, D. A., Gaub, H. E. et al. (2019). Structural and mechanistic insights into mechanoactivation of focal adhesion kinase. *Proc. Natl. Acad. Sci. USA* **116**, 6766-6774. doi:10.1073/pnas.1820567116

Betzig, E., Patterson, G. H., Sougrat, R., Lindwasser, O. W., Olenych, S., Bonifacino, J. S., Davidson, M. W., Lippincott-Schwartz, J. and Hess, H. F. (2006). Imaging intracellular fluorescent proteins at nanometer resolution. *Science* **313**, 1642-1645. doi:10.1126/science.1127344

Bhatt, A., Kaverina, I., Otey, C. and Huttenlocher, A. (2002). Regulation of focal complex composition and disassembly by the calcium-dependent protease calpain. *J. Cell Sci.* **115**, 3415-3425. doi:10.1242/jcs.115.17.3415

Bolte, S. and Cordelieres, F. P. (2006). A guided tour into subcellular colocalization analysis in light microscopy. *J. Microsc.* **224**, 213-232. doi:10.1111/j.1365-2818.2006.01706.x

Byron, A., Humphries, J. D., Bass, M. D., Knight, D. and Humphries, M. J. (2011). Proteomic analysis of integrin adhesion complexes. *Sci. Signal.* **4**, pt2. doi:10.1126/scisignal.2001827

Carisey, A., Tsang, R., Greiner, A. M., Nijenhuis, N., Heath, N., Nazgiewicz, A., Kemkemer, R., Derby, B., Spatz, J. and Ballestrem, C. (2013). Vinculin regulates the recruitment and release of core focal adhesion proteins in a force-dependent manner. *Curr. Biol.* **23**, 271-281. doi:10.1016/j.cub.2013.01.009

Cavalcanti-Adam, E. A., Volberg, T., Micoulet, A., Kessler, H., Geiger, B. and Spatz, J. P. (2007). Cell spreading and focal adhesion dynamics are regulated by spacing of integrin ligands. *Biophys. J.* **92**, 2964-2974. doi:10.1529/biophysj.106.089730

Changede, R., Xu, X., Margadant, F. and Sheetz, M. P. (2015). Nascent Integrin Adhesions Form on All Matrix Rigidities after Integrin Activation. *Dev. Cell* **35**, 614-621. doi:10.1016/j.devcel.2015.11.001

Chenouard, N., Buisson, J., Bloch, I., Bastin, P. and Olivo-Marin, J.-C. (2010). Curvelet analysis of kymograph for tracking bi-directional particles in fluorescence microscopy images. 17th IEEE International Conference on Image Processing (ICIP).

Chertkova, A. O., Mastop, M., Postma, M., van Bommel, N., van der Niet, S., Batenburg, K. L., Joosen, L., Gadella, T. W. J., Jr, Okada, Y. and Goedhart, J. (2020). Robust and bright genetically encoded fluorescent markers for highlighting structures and compartments in mammalian cells. *bioRxiv*, 160374. doi:10.1101/160374

Choi, C. K., Zareno, J., Digman, M. A., Gratton, E. and Horwitz, A. R. (2011). Cross-correlated fluctuation analysis reveals phosphorylation-regulated paxillin-FAK complexes in nascent adhesions. *Biophys. J.* **100**, 583-592. doi:10.1016/j.bpj.2010.12.3719

Conway, J. R. W. and Jacquemet, G. (2019). Cell matrix adhesion in cell migration. *Essays Biochem.* **63**, 535-551. doi:10.1042/EBC20190012

Culley, S., Albrecht, D., Jacobs, C., Pereira, P. M., Leterrier, C., Mercer, J. and Henriques, R. (2018). Quantitative mapping and minimization of super-resolution optical imaging artifacts. *Nat. Methods* **15**, 263-266. doi:10.1038/nmeth.4605

de Chaumont, F., Dallongeville, S., Chenouard, N., Hervé, N., Pop, S., Provoost, T., Meas-Yedid, V., Pankajakshan, P., Lecomte, T., Le Montagner, Y. et al. (2012). Icy: an open bioimage informatics platform for extended reproducible research. *Nat. Methods* **9**, 690-696. doi:10.1038/nmeth.2075

Deakin, N. O. and Turner, C. E. (2008). Paxillin comes of age. *J. Cell Sci.* **121**, 2435-2444. doi:10.1242/jcs.018044

Deramaudt, T. B., Dujardin, D., Hamadi, A., Noulet, F., Kolli, K., De Mey, J., Takeda, K. and Rondé, P. (2011). FAK phosphorylation at Tyr-925 regulates cross-talk between focal adhesion turnover and cell protrusion. *Mol. Biol. Cell* **22**, 964-975. doi:10.1091/mbc.e10-08-0725

Deramaudt, T. B., Dujardin, D., Noulet, F., Martin, S., Vauchelles, R., Takeda, K. and Rondé, P. (2014). Altering FAK-paxillin interactions reduces adhesion, migration and invasion processes. *PLoS ONE* **9**, e92059. doi:10.1371/journal.pone.0092059

Diez-Ahedo, R., Normanno, D., Esteban, O., Bakker, G.-J., Figdor, C. G., Cambi, A. and Garcia-Parajo, M. F. (2009). Dynamic re-organization of individual adhesion nanoclusters in living cells by ligand-patterned surfaces. *Small* **5**, 1258-1263. doi:10.1002/smll.200801699

Digman, M. A., Brown, C. M., Horwitz, A. R., Mantulin, W. W. and Gratton, E. (2008). Paxillin dynamics measured during adhesion assembly and disassembly by correlation spectroscopy. *Biophys. J.* **94**, 2819-2831. doi:10.1529/biophysj.107.104984

Digman, M. A., Wiseman, P. W., Choi, C., Horwitz, A. R. and Gratton, E. (2009). Stoichiometry of molecular complexes at adhesions in living cells. *Proc. Natl. Acad. Sci. USA* **106**, 2170-2175. doi:10.1073/pnas.0806036106

Franz, C. M. and Müller, D. J. (2005). Analyzing focal adhesion structure by atomic force microscopy. *J. Cell Sci.* **118**, 5315-5323. doi:10.1242/jcs.02653

Gardel, M. L., Schneider, I. C., Aratyn-Schaus, Y. and Waterman, C. M. (2010). Mechanical integration of actin and adhesion dynamics in cell migration. *Annu. Rev. Cell Dev. Biol.* **26**, 315-333. doi:10.1146/annurev.cellbio.011209.122036

Goddard, T. D., Huang, C. C., Meng, E. C., Pettersen, E. F., Couch, G. S., Morris, J. H. and Ferrin, T. E. (2018). UCSF ChimeraX: Meeting modern challenges in visualization and analysis. *Protein Sci.* **27**, 14-25. doi:10.1002/pro.3235

Goedhart, J. (2020). PlotTwist: a web app for plotting and annotating continuous data. *PLoS Biol.* **18**, e3000581. doi:10.1371/journal.pbio.3000581

Goedhart, J. (2021). SuperPlotsOfData-a web app for the transparent display and quantitative comparison of continuous data from different conditions. *Mol. Biol. Cell* **32**, 470-474. doi:10.1091/mbc.E20-09-0583

Grashoff, C., Hoffman, B. D., Brenner, M. D., Zhou, R., Parsons, M., Yang, M. T., McLean, M. A., Sligar, S. G., Chen, C. S., Ha, T. et al. (2010). Measuring mechanical tension across vinculin reveals regulation of focal adhesion dynamics. *Nature* **466**, 263-266. doi:10.1038/nature09198

Green, H. J. and Brown, N. H. (2019). Integrin intracellular machinery in action. *Exp. Cell Res.* **378**, 226-231. doi:10.1016/j.yexcr.2019.03.011

Gudzenko, T. and Franz, C. M. (2015). Studying early stages of fibronectin fibrillogenesis in living cells by atomic force microscopy. *Mol. Biol. Cell* **26**, 3190-3204. doi:10.1091/mbc.e14-05-1026

Gustafsson, N., Culley, S., Ashdown, G., Owen, D. M., Pereira, P. M. and Henriques, R. (2016). Fast live-cell conventional fluorophore nanoscopy with ImageJ through super-resolution radial fluctuations. *Nat. Commun.* **7**, 12471. doi:10.1038/ncomms12471

Hoellerer, M. K., Noble, M. E. M., Labesse, G., Campbell, I. D., Werner, J. M. and Arold, S. T. (2003). Molecular recognition of paxillin LD motifs by the focal adhesion targeting domain. *Structure* **11**, 1207-1217. doi:10.1016/j.str.2003.08.010

Hoffmann, J.-E., Fermin, Y., Stricker, R. L. O., Ickstadt, K. and Zamir, E. (2014). Symmetric exchange of multi-protein building blocks between stationary focal adhesions and the cytosol. *Elife* **3**, e02257. doi:10.7554/eLife.02257

Horton, E. R., Byron, A., Askari, J. A., Ng, D. H. J., Millon-Frémillon, A., Robertson, J., Koper, E. J., Paul, N. R., Warwood, S., Knight, D. et al. (2015). Definition of a consensus integrin adhesome and its dynamics during adhesion complex assembly and disassembly. *Nat. Cell Biol.* **17**, 1577-1587. doi:10.1038/ncb3257

Horton, E. R., Humphries, J. D., Stutchbury, B., Jacquemet, G., Ballestrem, C., Barry, S. T. and Humphries, M. J. (2016). Modulation of FAK and Src adhesion signaling occurs independently of adhesion complex composition. *J. Cell Biol.* **212**, 349-364. doi:10.1083/jcb.201508080

Howard, J., Grill, S. W. and Bois, J. S. (2011). Turing's next steps: the mechanochemical basis of morphogenesis. *Nat. Rev. Mol. Cell Biol.* **12**, 392-398. doi:10.1038/nrm3120

Hu, S., Tee, Y.-H., Kabla, A., Zaidel-Bar, R., Bershadsky, A. and Hersen, P. (2015). Structured illumination microscopy reveals focal adhesions are composed of linear subunits. *Cytoskeleton* **72**, 235-245. doi:10.1002/cm.21223

Humphries, J. D., Wang, P., Streuli, C., Geiger, B., Humphries, M. J. and Ballestrem, C. (2007). Vinculin controls focal adhesion formation by direct interactions with talin and actin. *J. Cell Biol.* **179**, 1043-1057. doi:10.1083/jcb.200703036

Ilić, D., Furuta, Y., Kanazawa, S., Takeda, N., Sobue, K., Nakatsuji, N., Nomura, S., Fujimoto, J., Okada, M. and Yamamoto, T. (1995). Reduced cell motility and enhanced focal adhesion contact formation in cells from FAK-deficient mice. *Nature* **377**, 539-544. doi:10.1038/377539a0

Ivarsson, Y., Wawrzyniak, A. M., Kashyap, R., Polanowska, J., Betzi, S., Lembo, F., Vermeiren, E., Chiheb, D., Lenfant, N., Morelli, X. et al. (2013). Prevalence, specificity and determinants of lipid-interacting PDZ domains from an in-cell screen and in vitro binding experiments. *PLoS ONE* **8**, e54581. doi:10.1371/journal.pone.0054581

Jacquemet, G., Carisey, A. F., Hamidi, H., Henriques, R. and Leterrier, C. (2020). The cell biologist's guide to super-resolution microscopy. *J. Cell Sci.* **133**, jcs240713. doi:10.1242/jcs.240713

Jumper, J., Evans, R., Pritzel, A., Green, T., Figurnov, M., Ronneberger, O., Tunyasuvunakool, K., Bates, R., Žídek, A., Potapenko, A. et al. (2021). Highly accurate protein structure prediction with AlphaFold. *Nature* **596**, 583-589. doi:10.1038/s41586-021-03819-2

Kadaré, G., Gervasi, N., Brami-Cherrier, K., Blockus, H., El Messari, S., Arold, S. T. and Girault, J.-A. (2015). Conformational dynamics of the focal adhesion targeting domain control specific functions of focal adhesion kinase in cells. *J. Biol. Chem.* **290**, 478-491. doi:10.1074/jbc.M114.593632

Kanchanawong, P., Shtengel, G., Pasapera, A. M., Ramko, E. B., Davidson, M. W., Hess, H. F. and Waterman, C. M. (2010). Nanoscale architecture of integrin-based cell adhesions. *Nature* **468**, 580-584. doi:10.1038/nature09621

Kuo, J.-C., Han, X., Hsiao, C.-T., Yates, J. R., III and Waterman, C. M. (2011). Analysis of the myosin-II-responsive focal adhesion proteome reveals a role for β-Pix in negative regulation of focal adhesion maturation. *Nat. Cell Biol.* **13**, 383-393. doi:10.1038/ncb2216

Laine, R. F., Tosheva, K. L., Gustafsson, N., Gray, R. D. M., Almada, P., Albrecht, D., Risa, G. T., Hurtig, F., Lindås, A.-C., Baum, B. et al. (2019). NanoJ: a high-performance open-source super-resolution microscopy toolbox. *J. Phys. D Appl. Phys.* **52**, 163001. doi:10.1088/1361-6463/ab0261

Liu, J., Wang, Y., Goh, W. I., Goh, H., Baird, M. A., Ruehland, S., Teo, S., Bate, N., Critchley, D. R., Davidson, M. W. et al. (2015). Talin determines the nanoscale architecture of focal adhesions. *Proc. Natl. Acad. Sci. USA* **112**, E4864-E4873. doi:10.1073/pnas.1512025112

Mierke, C. T., Kollmannsberger, P., Zitterbart, D. P., Diez, G., Koch, T. M., Marg, S. and . . Fabry, B. (2010). Vinculin facilitates cell invasion into three-dimensional collagen matrices. *J. Biol. Chem.* **285**, 13121-13130. doi:10.1074/jbc.M109.087171

Mirdita, M., Ovchinnikov, S. and Steinegger, M. (2021). ColabFold - making protein folding accessible to all. *bioRxiv*, 2021.2008.2015.456425. doi:10.1101/2021.08.15.456425

Mousson, A., Legrand, M., Steffan, T., Vauchelles, R., Carl, P., Gies, J.-P., Lehmann, M., Zuber, G., De Mey, J., Dujardin, D. et al. (2021). Inhibiting FAK-paxillin interaction reduces migration and invadopodia-mediated matrix degradation in metastatic melanoma cells. *Cancers (Basel)* **13**, 1871. doi:10.3390/cancers13081871

Pasapera, A. M., Schneider, I. C., Rericha, E., Schlaepfer, D. D. and Waterman, C. M. (2010). Myosin II activity regulates vinculin recruitment to focal adhesions through FAK-mediated paxillin phosphorylation. *J. Cell Biol.* **188**, 877-890. doi:10.1083/jcb.200906012

Patla, I., Volberg, T., Elad, N., Hirschfeld-Warneken, V., Grashoff, C., Fässler, R., Spatz, J. P., Geiger, B. and Medalia, O. (2010). Dissecting the molecular architecture of integrin adhesion sites by cryo-electron tomography. *Nat. Cell Biol.* **12**, 909-915. doi:10.1038/ncb2095

Petit, V., Boyer, B., Lentz, D., Turner, C. E., Thiery, J. P. and Vallés, A. M. (2000). Phosphorylation of tyrosine residues 31 and 118 on paxillin regulates cell migration through an association with CRK in NBT-II cells. *J. Cell Biol.* **148**, 957-970. doi:10.1083/jcb.148.5.957

Pettersen, E. F., Goddard, T. D., Huang, C. C., Meng, E. C., Couch, G. S., Croll, T. I., Morris, J. H. and Ferrin, T. E. (2021). UCSF ChimeraX: structure visualization for researchers, educators, and developers. *Protein Sci.* **30**, 70-82. doi:10.1002/pro.3943

Pinon, P., Pärssinen, J., Vazquez, P., Bachmann, M., Rahikainen, R., Jacquier, M.-C., Azizi, L., Määttä, J. A., Bastmeyer, M., Hytönen, V. P. et al. (2014). Talin-bound NPLY motif recruits integrin-signaling adapters to regulate cell spreading and mechanosensing. *J. Cell Biol.* **205**, 265-281. doi:10.1083/jcb.201308136

Ripamonti, M., Liaudet, N., Azizi, L., Bouvard, D., Hytönen, V. P. and Wehrle-Haller, B. (2021). Structural and functional analysis of LIM domain-dependent recruitment of paxillin to αvβ3 integrin-positive focal adhesions. *Commun. Biol.* **4**, 380. doi:10.1038/s42003-021-01886-9

Saltel, F., Mortier, E., Hytönen, V. P., Jacquier, M.-C., Zimmermann, P., Vogel, V., Liu, W. and Wehrle-Haller, B. (2009). New PI(4,5)P2- and membrane proximal integrin-binding motifs in the talin head control beta3-integrin clustering. *J. Cell Biol.* **187**, 715-731. doi:10.1083/jcb.200908134

Schaller, M. D. and Parsons, J. T. (1995). pp125FAK-dependent tyrosine phosphorylation of paxillin creates a high-affinity binding site for Crk. *Mol. Cell. Biol.* **15**, 2635-2645. doi:10.1128/MCB.15.5.2635

Schiller, H. B., Friedel, C. C., Boulegue, C. and Fässler, R. (2011). Quantitative proteomics of the integrin adhesome show a myosin II-dependent recruitment of LIM domain proteins. *EMBO Rep.* **12**, 259-266. doi:10.1038/embor.2011.5

Schindelin, J., Rueden, C. T., Hiner, M. C. and Eliceiri, K. W. (2015). The ImageJ ecosystem: an open platform for biomedical image analysis. *Mol. Reprod. Dev.* **82**, 518-529. doi:10.1002/mrd.22489

Seong, J., Tajik, A., Sun, J., Guan, J. L., Humphries, M. J., Craig, S. E., Shekaran, A., García, A. J., Lu, S., Lin, M. Z. et al. (2013). Distinct biophysical mechanisms of focal adhesion kinase mechanoactivation by different extracellular matrix proteins. *Proc. Natl. Acad. Sci. USA* **110**, 19372-19377. doi:10.1073/pnas.1307405110

Shroff, H., Galbraith, C. G., Galbraith, J. A., White, H., Gillette, J., Olenych, S., Davidson, M. W. and Betzig, E. (2007). Dual-color superresolution imaging of genetically expressed probes within individual adhesion complexes. *Proc. Natl. Acad. Sci. USA* **104**, 20308-20313. doi:10.1073/pnas.0710517105

Shroff, H., Galbraith, C. G., Galbraith, J. A. and Betzig, E. (2008). Live-cell photoactivated localization microscopy of nanoscale adhesion dynamics. *Nat. Methods* **5**, 417-423. doi:10.1038/nmeth.1202

Soto-Ribeiro, M., Kastberger, B., Bachmann, M., Azizi, L., Fouad, K., Jacquier, M.-C., Boettiger, D., Bouvard, D., Bastmeyer, M., Hytönen, V. P. et al. (2019). β1D integrin splice variant stabilizes integrin dynamics and reduces integrin signaling by limiting paxillin recruitment. *J. Cell Sci.* **132**, jcs224493. doi:10.1242/jcs.224493

Spiess, M., Hernandez-Varas, P., Oddone, A., Olofsson, H., Blom, H., Waithe, D., Lock, J. G., Lakadamyali, M. and Strömblad, S. (2018). Active and inactive β1 integrins segregate into distinct nanoclusters in focal adhesions. *J. Cell Biol.* **217**, 1929-1940. doi:10.1083/jcb.201707075

Sulzmaier, F. J., Jean, C. and Schlaepfer, D. D. (2014). FAK in cancer: mechanistic findings and clinical applications. *Nat. Rev. Cancer* **14**, 598-610. doi:10.1038/nrc3792

Sun, X., Phua, D. Y. Z., Axiotakis, L., Smith, M. A., Blankman, E., Gong, R., Cail, R. C., Espinosa de los Reyes, S., Beckerle, M. C., Waterman, C. M. et al. (2020). Mechanosensing through Direct Binding of Tensed F-Actin by LIM Domains. *Dev. Cell* **55**, 468-482.e67. doi:10.1016/j.devcel.2020.09.022

Theodosiou, M., Widmaier, M., Böttcher, R. T., Rognoni, E., Veelders, M., Bharadwaj, M., Lambacher, A., Austen, K., Müller, D. J., Zent, R. et al. (2016). Kindlin-2 cooperates with talin to activate integrins and induces cell spreading by directly binding paxillin. *Elife* **5**, e10130. doi:10.7554/eLife.10130

Thievessen, I., Thompson, P. M., Berlemont, S., Plevock, K. M., Plotnikov, S. V., Zemljic-Harpf, A., Ross, R. S., Davidson, M. W., Danuser, G., Campbell, S. L. et al. (2013). Vinculin-actin interaction couples actin retrograde flow to focal adhesions, but is dispensable for focal adhesion growth. *J. Cell Biol.* **202**, 163-177. doi:10.1083/jcb.201303129

Thomas, J. W., Ellis, B., Boerner, R. J., Knight, W. B., White, G. C., II and Schaller, M. D. (1998). SH2- and SH3-mediated interactions between focal adhesion kinase and Src. *J. Biol. Chem.* **273**, 577-583. doi:10.1074/jbc.273.1.577

Thomas, J. W., Cooley, M. A., Broome, J. M., Salgia, R., Griffin, J. D., Lombardo, C. R. and Schaller, M. D. (1999). The role of focal adhesion kinase binding in the regulation of tyrosine phosphorylation of paxillin. *J. Biol. Chem.* **274**, 36684-36692. doi:10.1074/jbc.274.51.36684

Torsoni, A. S., Constancio, S. S., Nadruz, W., Hanks, S. K. and Franchini, K. G. (2003). Focal adhesion kinase is activated and mediates the early hypertrophic response to stretch in cardiac myocytes. *Circ. Res.* **93**, 140-147. doi:10.1161/01.RES.0000081595.25297.1B

Winkelman, J. D., Anderson, C. A., Suarez, C., Kovar, D. R. and Gardel, M. L. (2020). Evolutionarily diverse LIM domain-containing proteins bind stressed actin filaments through a conserved mechanism. *Proc. Natl. Acad. Sci. USA* **117**, 25532-25542. doi:10.1073/pnas.2004656117

Wong, V. W., Rustad, K. C., Akaishi, S., Sorkin, M., Glotzbach, J. P., Januszyk, M., Nelson, E. R., Levi, K., Paterno, J., Vial, I. N. et al. (2011). Focal adhesion kinase links mechanical force to skin fibrosis via inflammatory signaling. *Nat. Med.* **18**, 148-152. doi:10.1038/nm.2574

Xu, L., Braun, L. J., Rönnlund, D., Widengren, J., Aspenström, P. and Gad, A. K. B. (2018). Nanoscale localization of proteins within focal adhesions indicates discrete functional assemblies with selective force-dependence. *FEBS J.* **285**, 1635-1652. doi:10.1111/febs.14433

Young, L. E. and Higgs, H. N. (2018). Focal Adhesions Undergo Longitudinal Splitting into Fixed-Width Units. *Curr. Biol.* **28**, 2033-2045.e35. doi:10.1016/j.cub.2018.04.073

Zaidel-Bar, R., Milo, R., Kam, Z. and Geiger, B. (2007). A paxillin tyrosine phosphorylation switch regulates the assembly and form of cell-matrix adhesions. *J. Cell Sci.* **120**, 137-148. doi:10.1242/jcs.03314

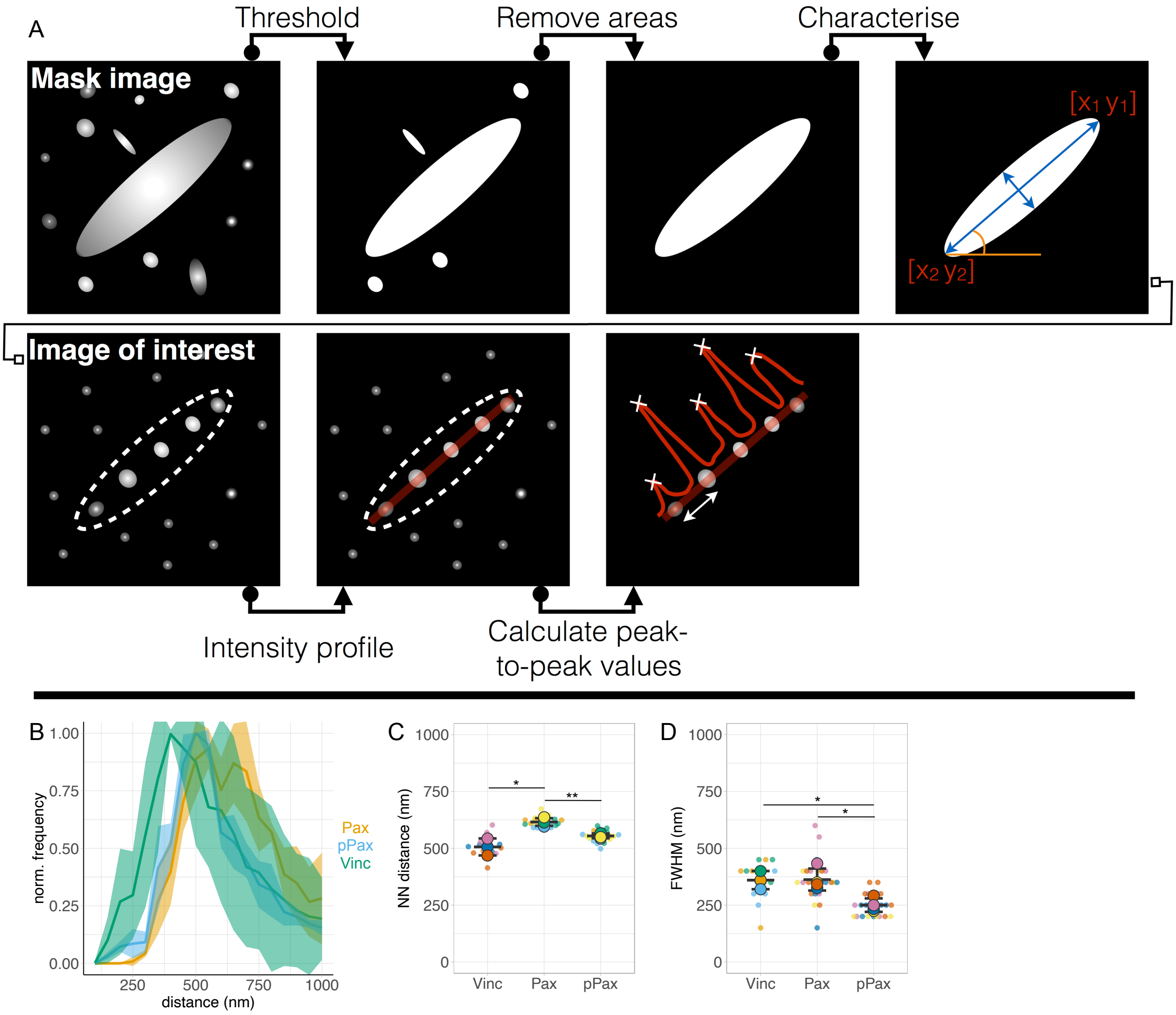

Fig. S1. (A) Scheme of the analysis for the spacing between pPax-Y118 clusters as shown in Figure 2. An image of paxillin staining (first row) is used as a mask for the subsequent analysis of the pPax-Y118 staining (second row). The paxillin staining is thresholded and objects smaller than focal adhesions (1-3 μm^2) are discarded. This image is used as a mask for the corresponding pPax-Y118 staining (second row). Then, the intensity profile within the masked area is measured and the peaks of the intensity profile are calculated. The distance between these peaks yields the center-to-center distance of pPax-Y118 clusters. (B-D) Analysis of REF cells labeled for vinculin (N=3, n=15) and comparison to data for paxillin and pPax-Y118 shown in Fig. 2B-D. (B,C) Maxima of vinculin labeling are closer to each other compared to maxima of paxillin and pPax-Y118 but (B,D) their distribution is broad as seen for paxillin and not restricted as observed for pPax-Y118. Significance was tested between all conditions based on independent experiments with Welch's t-test after testing for normal distribution with Shapiro-Wilk test. *: 0.05 >= p > 0.01; **: 0.01 >= p > 0.001; ***: p <= 0.001.

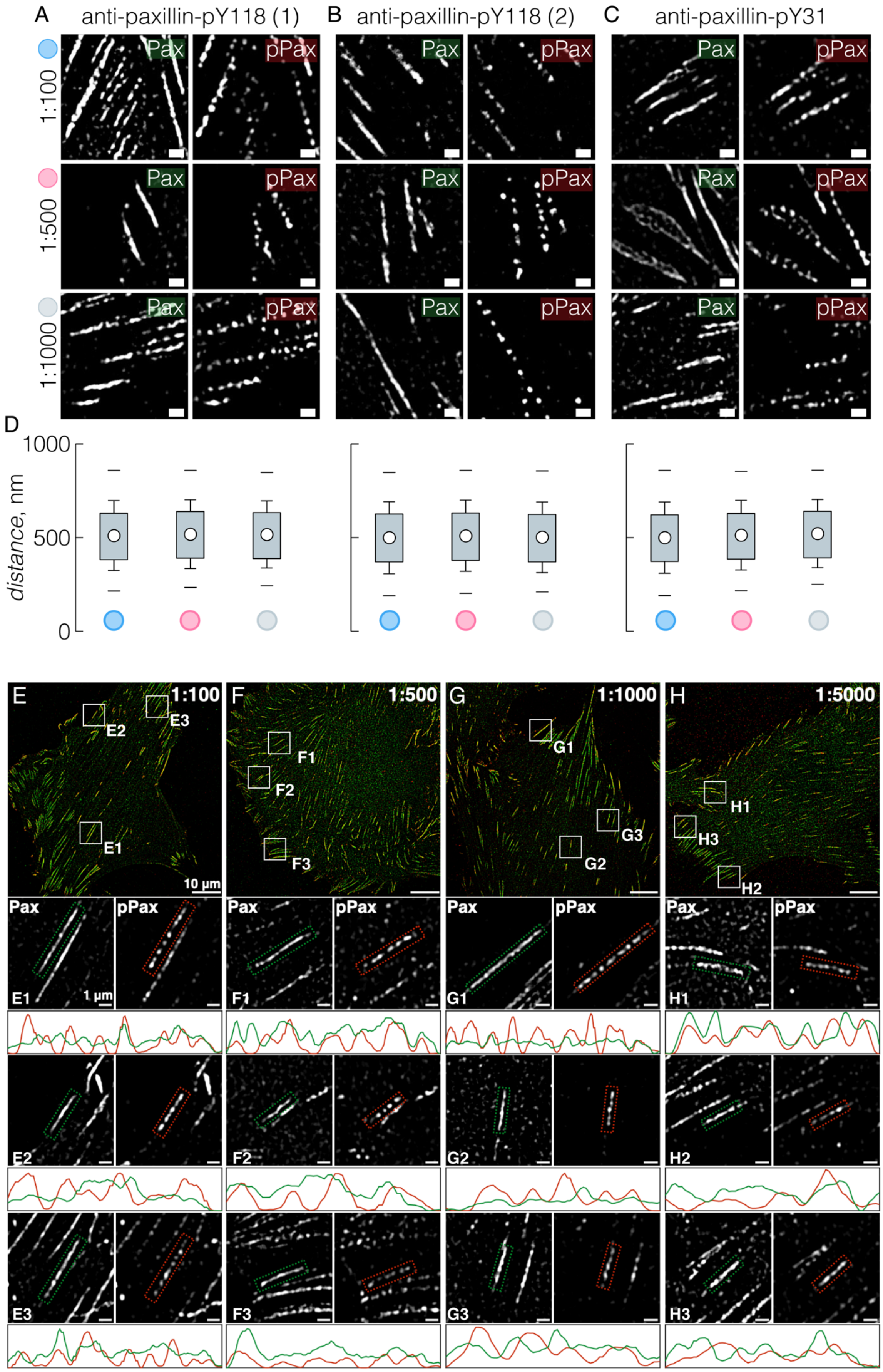
A
anti-paxillin-pY118 (1)
B
anti-paxillin-pY118 (2)
C
anti-paxillin-pY31
1:100
1:500
1:1000
Pax
pPax
D
distance, nm
1000
500
0
E
1:100
E1
E2
E3
10 µm
F
1:500
F1
F2
F3
G
1:1000
G1
G2
G3
H
1:5000
H1
H2
H3
1 µm

Fig. S2. Clustering of pPax-Y118 is irrespective of primary antibodies and phosphorylation sites. REF cells were labeled with primary antibodies for paxillin

(green); dilution 1:500 for all conditions. (A-B) pPax-Y118 was labeled with two different antibodies; (A) antibody used throughout this study or (B) antibody from another distributor. (C) Staining for pPax-Y31. (A-C) Primary antibodies against pPax-Y118 or pPax-Y31 were diluted as indicated on the left. (D) Distance analysis for all different primary pPax antibodies and for all dilutions tested showed no significant effect of primary antibody or dilution (matlab workflow; N = 3, n = 13). Scale bars: always 1 µm. Significance was tested between all conditions based on independent experiments with Welch's t-test after testing for normal distribution with Shapiro-Wilk test. No significant difference was detected. (E-H) REF cells labeled with primary antibodies for paxillin (green) and for pPax-Y118 (red). Primary antibodies for pPax-Y118 were always diluted 1:500. Primary antibody for paxillin was diluted: (E) 1:100, (F) 1:500, (G) 1:1000, and (H) 1:5000. Paxillin always appeared homogeneous in focal adhesions while pPax-Y118 appeared in spots. Scale bars: (E-H) 10 µm, (E1-H3) 1 µm.

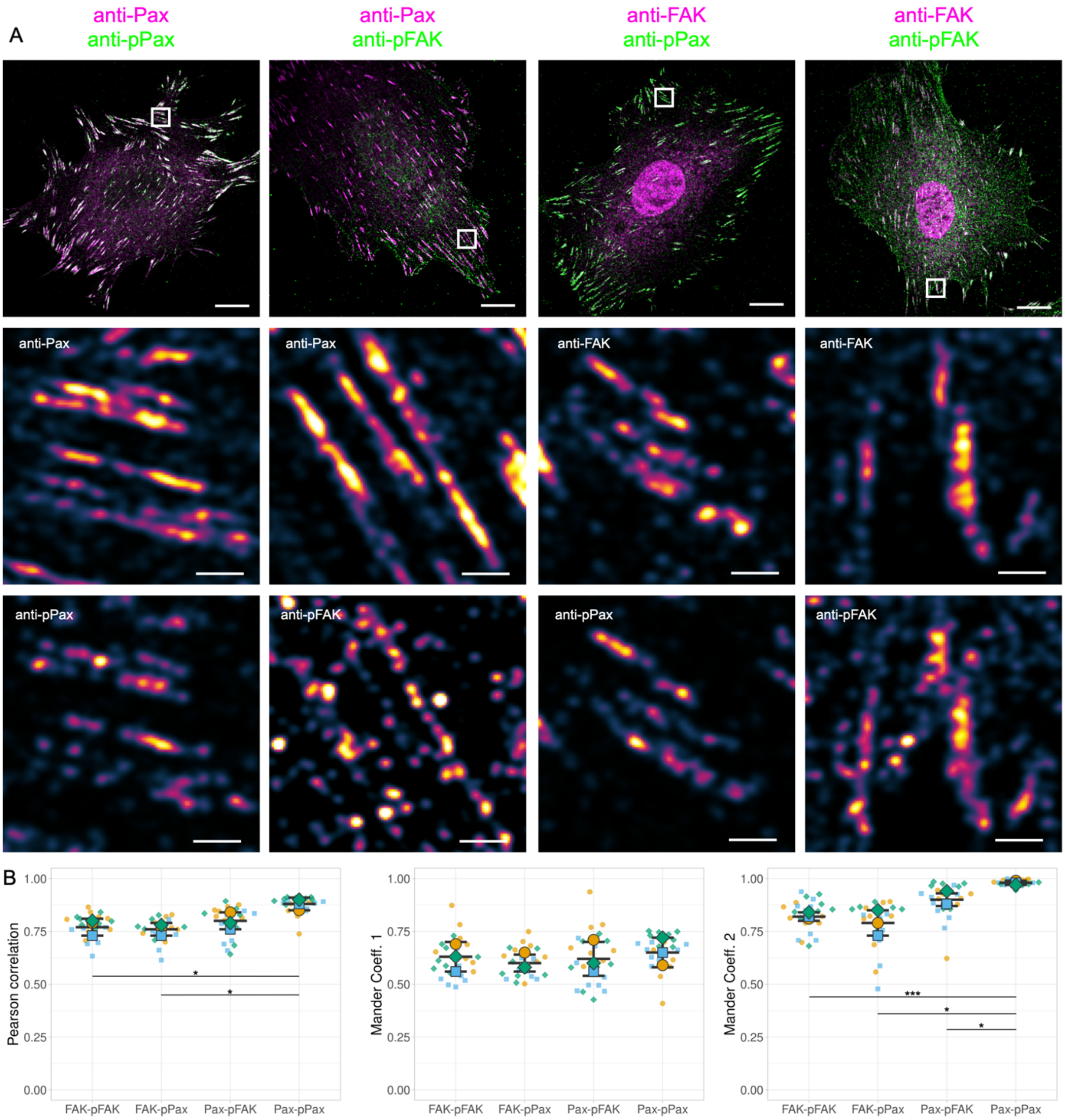

Fig. S3. Correlation and co-occurrence of pFAK, pPax, FAK, and Pax. (A) REF cells labeled for either FAK or Pax and for either pFAK or pPax as indicated. (B) FAK or Pax signal was used to create a mask to isolate focal adhesions and to restrict analysis to focal adhesion area. Pearson correlation and Mander coefficients were analyzed with ImageJ plugin “JACoP” (Bolte & Cordelieres, 2006); Mander coefficient was analyzed after applying a threshold (level by using Otsu method, automatic detection). Mander coefficient 1 indicates ratio of FAK or Pax that overlaps with pFAK or pPax. Mander coefficient 2 indicates ratio of pFAK or pPax that overlaps with FAK or Pax. Bars indicate mean and standard deviation, small dots single cells, big dots averages from independent experiments (N = 3, at least 23 cells were analyzed per condition). Scale bars: 10 µm in overview pictures, 1 µm in zoom ins. Significance was tested between all conditions based on independent experiments with Welch’s t-test after testing for normal distribution with Shapiro-Wilk test. *: 0.05 >= p > 0.01; **: 0.01 >= p > 0.001; ***: p <= 0.001.

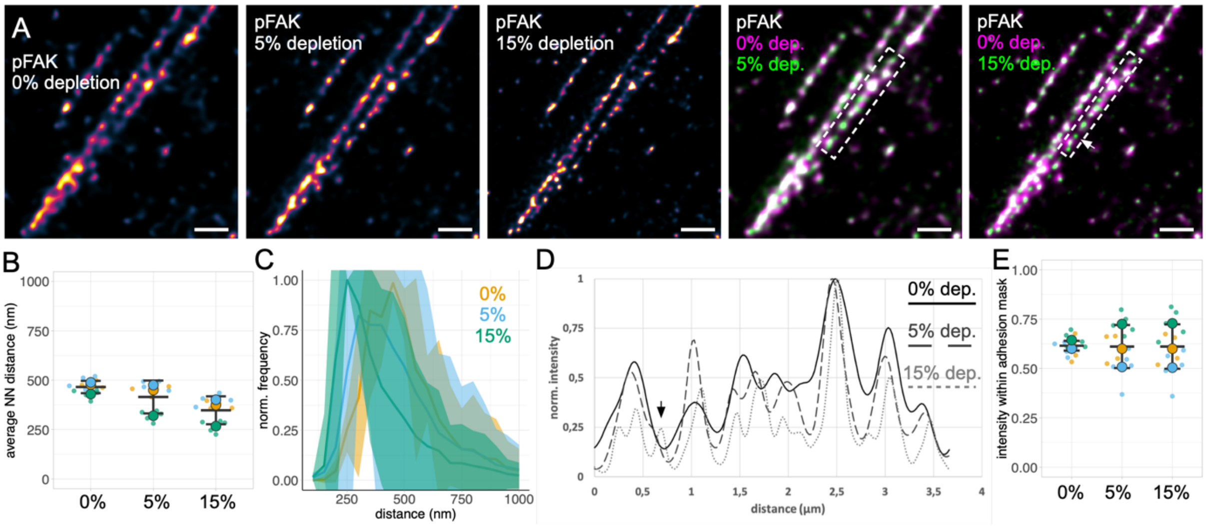

Fig. S4. STED imaging resolves spatial clusters of pFAK. (A) Fixed NIH3T3 cells labeled for pFAK and imaged with STED. Different intensities of STED depletion laser were used to achieve resolution of confocal microscopy, SIM microscopy, or to resolve below these techniques (pixel sizes: 0%: 77x77 nm; 5%: 42x42 nm; 15%: 27x27 nm; expected resolution limit: 0%: 190 nm; 5%: 105 nm; 15%: 68 nm). Two pictures on the right show overlays of two different resolution condition for comparison; colors as indicated. (B) Average NN distances from NN analysis of pFAK imaged with respective condition (N = 3, n = 14). (C) Histogram based distance distribution plot. (D) Intensity profile for dashed white rectangle in overlay pictures in (A). Arrows in (A) and (D) highlight comparably dim pFAK structure that is not resolved with 0% and 5% depletion laser. (E) Analysis for amount of intensity detected at 0% depletion laser. An adhesion mask was created in images obtained with 0% depletion laser and applied to all conditions. Ratio of intensity inside this mask compared to complete intensity was calculated and plotted. Analysis indicates that adhesion area resolved at 0% depletion laser contains in average 62% of pFAK intensity. The same area contains 61% of pFAK intensity resolved with 5% depletion laser and 61% of pFAK intensity resolved with 15% depletion laser. Thus, 0% depletion laser captures the amount of labeled proteins within adhesions sufficiently. Scale bars: (A) 1 µm. Significance was tested between all conditions based on independent experiments with Welch’s t-test after testing for normal distribution with Shapiro-Wilk test. No significant difference was detected.

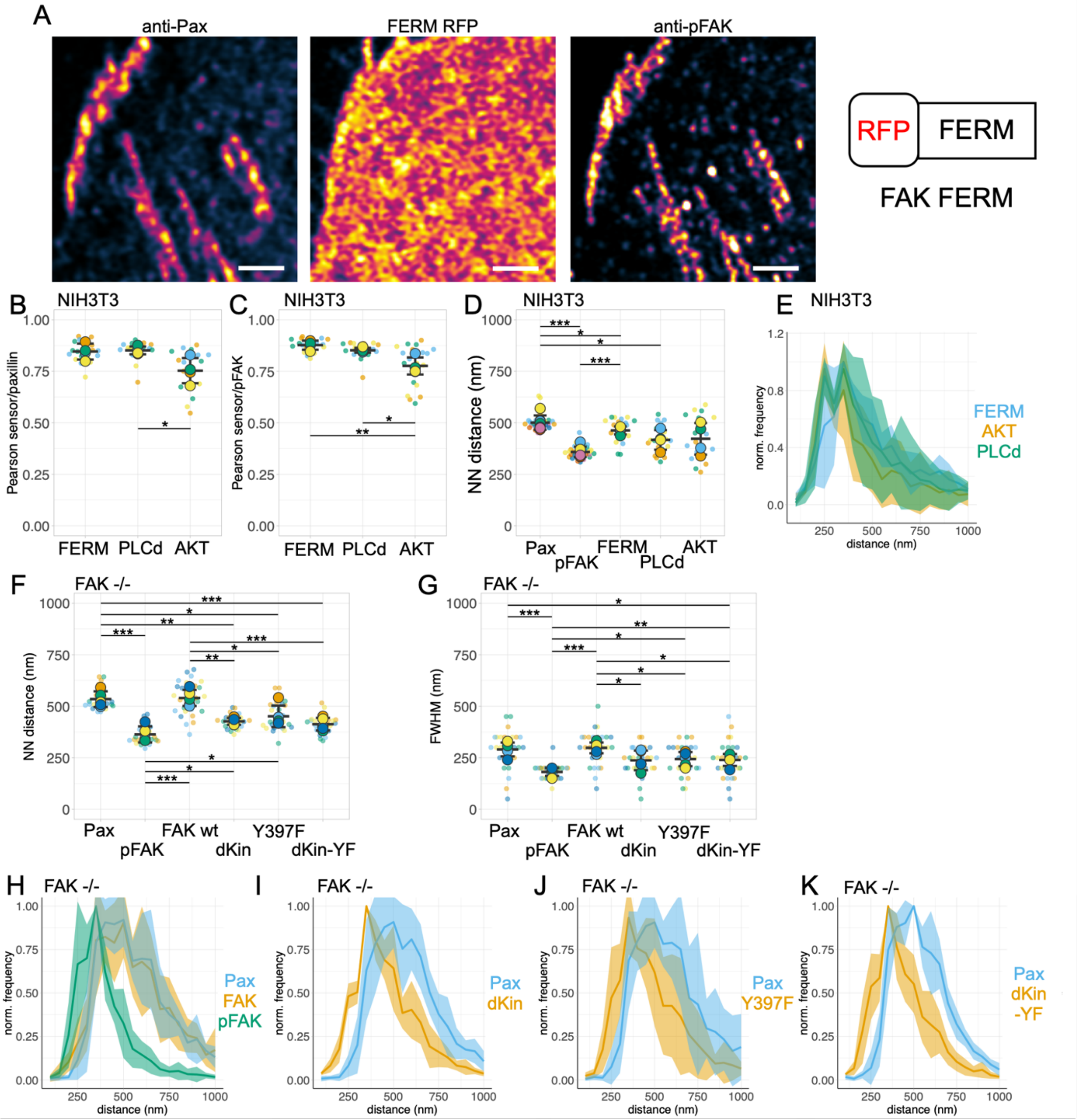

Fig. S5. (A-E) Analysis of correlation of spatial distribution of lipid sensors. Cells were transfected with lipid sensors (FAK FERM domain of FAK, PLCd PH, or AKT PH) and labeled for endogenous paxillin and pFAK (N = 4, 19-20 cells analyzed per condition). (B) Pearson intensity correlation between respective lipid sensor and paxillin and (C) lipid sensor and pFAK. Correlation was only measured for adhesions identified with pFAK labeling in order to focus on FAK recruitment to lipids as cause for pFAK distribution. (D-E) Distance distribution analysis with NN method for distribution of lipid sensors. Data for paxillin and pFAK in (D) is replotted from Fig. 5E. (F-K) MEF FAK -/- were transfected with FAK wt, FAK dKin, FAK Y397F, or FAK dKin Y397F. pFAK and endogenous paxillin was labeled with immunostaining (N= 5, at least 25 cells were analyzed per condition). (F) Distances between clusters detected with NN method. Data for paxillin and pFAK from FAK wt transfected cells and for respective FAK construct. (G) FWHM from histogram-based distance distribution plots. (H-K) Distance distribution plots for indicated FAK construct and paxillin (and pFAK for FAK wt). Scale bars: 1 µm. Significance was tested between all conditions based on independent experiments with Welch's t-test after testing for normal distribution with Shapiro-Wilk test. *: 0.05 >= p > 0.01; **: 0.01 >= p > 0.001; ***: p <= 0.001.

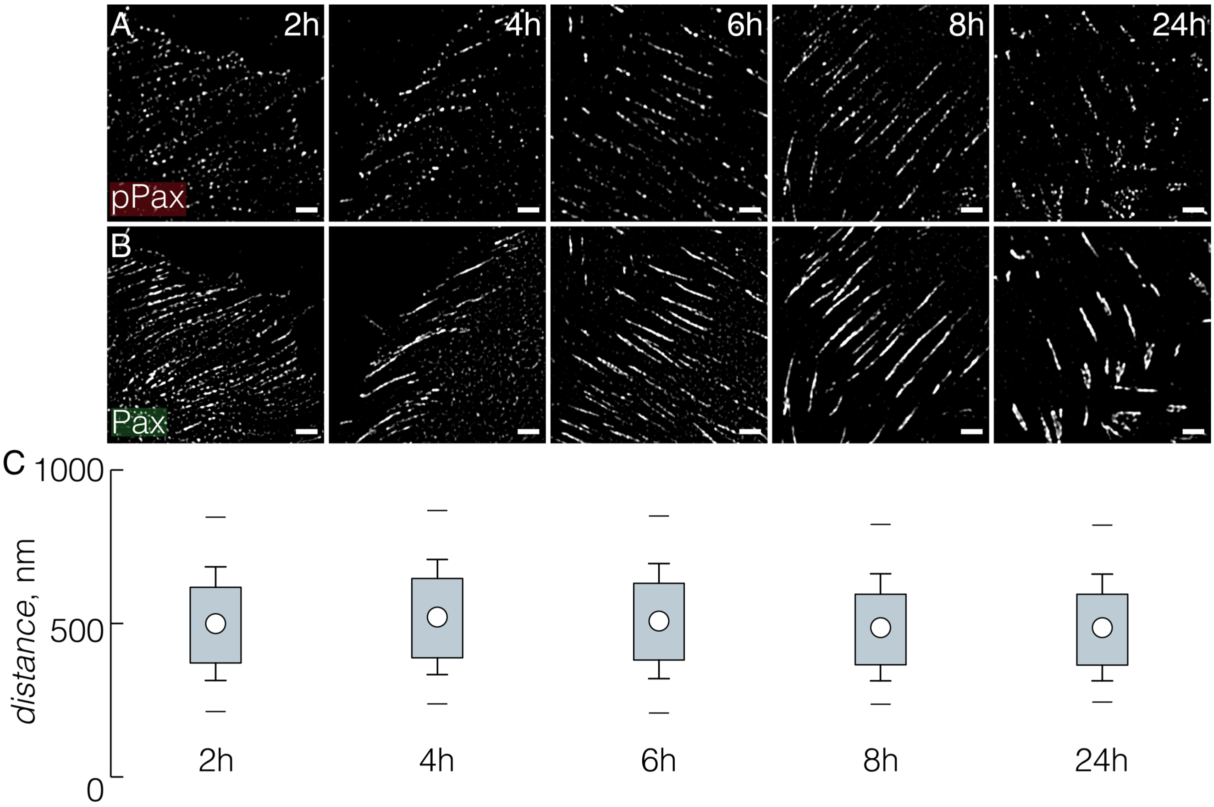

Fig. S6. Average distances between neighbored pPax-Y118 clusters show no time dependency. (A) REF cells cultured on fibronectin-coated coverslips and fixed at the indicated time point and stained for paxillin (green) and pPax-Y118 (red). (A) pPax-Y118 staining revealed spot-like patterns for all time points while (B) paxillin staining persisted throughout the long axis of focal adhesions. (C) Distance analysis for all time points showed no significant differences in pPax-Y118 spacing for time points analyzed (N=3, at least 15 cells per condition). No significant changes were detected (Welch's t-test after Shapiro-Wilk test). Scale bar: 2 μm.

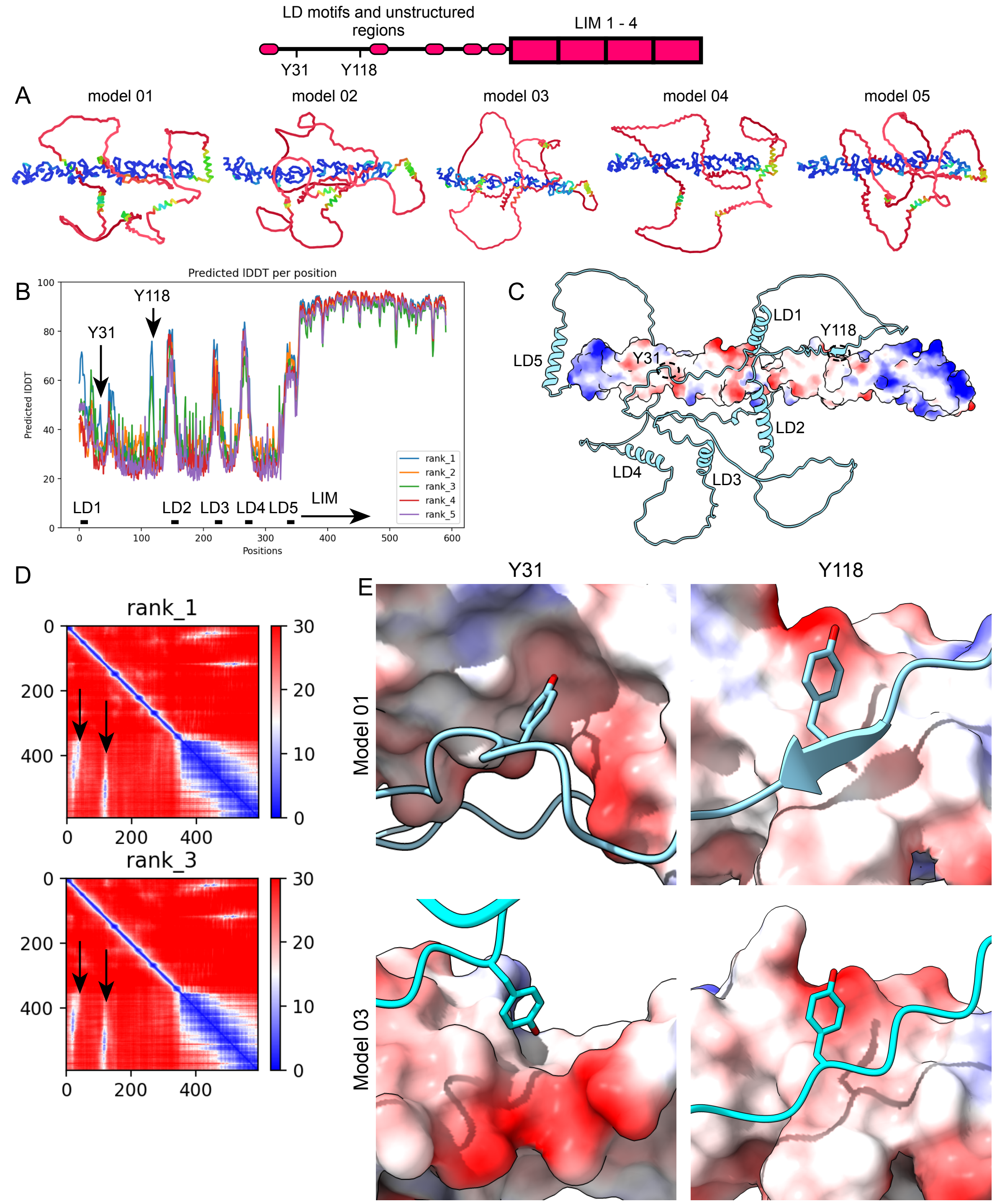

Fig. S7. (A) 5 models of human paxillin structure predicted with AlphaFold (Jumper et al., 2021) and ColabFold (Mirdita et al., 2021); MSA alignment was performed with Jackhmmer. Models are ordered according to model confidence (pLDDT score; model 01 with highest confidence). Color code indicates model confidence (blue: high confidence, red: low confidence). LIM and LD domains have high confidence, flexible regions have low confidence. (B) Plot of pLDDT score for all 5 models. Positions of LD and LIM domains are indicated with black bars at bottom of plot. Please note that only model 01 and model 03 have high pLDDT score at position of Y31 and of Y118. (C) Model 01 shown with electrostatic surface rendering for LIM domains (blue: positive charge, red: negative charge), and LD domains as helices and flexible domains in cyan. (D) Predicted Alignment Error for model01 (rank_1) and 03 (rank_3). Arrows highlight position of Y31 and Y118 with regard to x axis. Blue indicates low error when mapping position y of a true structure onto position x of a predicted structure. Meaning here that relative position of LIM domains (360 and higher on y-axis) in regards to x-positions of Y31 and Y118 is predicted with low error. Thus, positioning of Y31 and Y118 on surface of LIM domains as shown in model 01 and model 03 is more likely compared to their positioning in model 02, 04, and 05. (E) Closer inspection reveals that model 01 and model 03 locate Y31 and Y118 on the surface of LIM domains, close to negatively charged patches.